

# The Luminosity Function of the Hot and Cold Kuiper belt Populations

Wesley C. Fraser<sup>a</sup>, Michael E. Brown<sup>a</sup>, Megan E. Schwamb<sup>a</sup>

<sup>a</sup>*Division of Geological and Planetary Sciences, MS150-21, California Institute of Technology, 1200 E. California Blvd. Pasadena, CA 91101 USA*

---

## Abstract

We have performed an ecliptic survey of the Kuiper belt, with an areal coverage of 8.9 square degrees to a 50% limiting magnitude of  $r'_{Sloan} = 24.7$ , and have detected 88 Kuiper belt objects, roughly half of which received follow-up one to two months after detection. Using this survey data alone, we have measured the luminosity function of the Kuiper belt, thus avoiding any biases that might come from the inclusion of other observations. We have found that the *Cold* population defined as having inclinations less than  $5^\circ$  has a luminosity function slope  $\alpha_{Cold} = 0.82 \pm 0.23$ , and is different from the *Hot* population, which has inclinations greater than  $5^\circ$  and a luminosity function slope  $\alpha_{Hot} = 0.35 \pm 0.21$ . As well, we have found that those objects closer than 38 AU have virtually the same luminosity function slope as the *Hot* population. This result, along with similar findings of past surveys demonstrates that the dynamically cold Kuiper belt objects likely have a steep size distribution, and are unique from all of the excited populations which have much shallower distributions. This suggests that the dynamically excited population underwent a different accretion history and achieved a more evolved state of accretion than the cold population. As well, we discuss the similarities of the *Cold* and *Hot* populations with the size distributions of other planetesimal populations. We find that while the Jupiter family comets and the scattered disk exhibit similar size distributions, a power-law extrapolation to small sizes for the scattered disk cannot account for the observed influx of comets. As well, we have found that the Jupiter Trojan and *Hot* populations cannot have originated from the same parent population, a result that is difficult to reconcile with scattering models similar to the NICE model. We conclude that the similarity between the size distributions of the *Cold* population and the Jupiter Trojan population is a striking coincidence.

*Keywords:* Kuiper Belt Centaurs Trojan asteroids Accretion

---

## 1. Introduction

The size distribution is one of the most fundamental properties of a planetesimal population. As the size of an object is primarily determined from its accretion and collisional disruption histories, the size distribution can reveal important information on the accretion and collisional history of that population (for a recent example, see Bottke et al., 2005).

Unlike the closer populations such as the asteroid belt, whose proximity has allowed the accurate measurement of their size distributions (see for example Jedicke and Metcalfe, 1998; Jewitt et al.,

2000), the distance to the Kuiper belt has prevented an equally detailed determination of its size distribution. Observations thus far have demonstrated that for the Kuiper belt as a whole, the size distribution for objects with diameters,  $D \gtrsim 200$  km, is well described by a power-law. At some size  $50 \lesssim D \lesssim 150$  km, the size distribution rolls-over to a shallower distribution (Bernstein et al., 2004; Fuentes et al., 2009; Fraser and Kavelaars, 2009). Smaller than the roll-over, the size distribution appears to remain shallow to objects as small as  $D \sim 1$  km (Schlichting et al., 2009).

While the accuracy of current measurements prevents a detailed modelling of the history of objects in the region, some insight has already been gained. The steepness of the large object size distribution implies that for this population, ac-

---

\*Accepted by Icarus August 2nd, 2010.

*Email address:* fraserw@gps.caltech.edu (Wesley C. Fraser )

cretion was a short-lived phenomenon, likely not more than a few 100 Myr (Gladman et al., 2001; Kenyon, 2002; Fraser et al., 2008). The paucity of the observed belt, and the existence of the largest known members demonstrates that the belt has undergone significant mass depletion, losing as much or more than 99% of its primordial mass (Stern and Colwell, 1997; Kenyon and Luu, 1998; Jewitt and Sheppard, 2002; Fuentes et al., 2009). The existence of the roll-over at sizes larger than  $D \gtrsim 50$  km suggests that the belt has undergone significant collisional comminution in a region of significantly increased density compared to today (Kenyon and Bromley, 2004; Benavidez and Campo Bagatin, 2009; Fraser, 2009).

As well, recent observations have suggested that the size distribution of those dynamically cold (low inclinations and eccentricities) Kuiper belt objects is different than that of the dynamically hot (large inclinations and eccentricities) population (Levison and Stern, 2001). Bernstein et al. (2004) found that the size distribution of objects with inclinations,  $i < 5^\circ$  was steeper than the size distribution of objects with  $i > 5^\circ$ . Fuentes and Holman (2008) found similar results showing that the cold population had a steeper slope than the mixed populations as a whole. This result implies that the hot and cold populations are genetically separate populations, that have significantly different accretion and evolution histories.

The results of Bernstein et al. (2004) were drawn from samples of objects compiled from many different surveys. This practice was necessitated by available data. All surveys had either shallow limiting magnitudes and a large areal coverage, or vice-versa. The result was that most surveys did not have a sufficient range of objects for which the size distribution could be accurately measured from that survey alone. The practice of using data from multiple surveys opens the results to the possibility of being affected by calibration issues and variations in sky density which could lead to an incorrect measurement of the size distribution. When these effects were properly accounted for, Fraser et al. (2008); Fraser and Kavelaars (2009) found that these data could not be used to reliably test differences in subpopulations of the Kuiper belt.

Here we present the results of a new Kuiper belt survey. By virtue of the survey's design, a large number of objects were discovered and followed to

determine their inclinations, over a range of sizes sufficient to measure the size distribution for the hot and cold population without the use of other surveys. In Section 2 we present our observations, and our data reductions and discovery techniques. In Section 3 we present the analysis of our results, in Section 4 we discuss the implications of our results, and we end with concluding remarks in Section 5.

## 2. Observations and Reductions

### 2.1. Discovery Observations

The discovery observations were made on October 18, 2009 (UT) with Suprime-cam on the 8.2 m Subaru telescope (Miyazaki et al., 2002). Suprime-cam is 10-chip mosaic camera, with a field-of-view of roughly  $34' \times 27'$  with  $\sim 15''$  chip-gaps, and has a pixel scale of  $0.2''$ . The observations consisted imaging 34 fields, each visited three times in the  $r'$  filter with the camera long axis oriented horizontally in RA, with each visit consisting of a single 200 s exposure. The first and last images of a field were separated by roughly 6.5 hours. The observed fields were all within  $\sim 1.5^\circ$  of the ecliptic and within  $\sim 10^\circ$  of opposition at the discovery epoch. The total areal coverage of our survey after accounting for chip-gaps was 8.93 square degrees. Details of the individual fields are shown in Table 1 and Figure 1. The observations included multiple images of the D1 and D4 fields of the Canada-France-Hawaii Telescope Supernova Legacy Survey (Astier et al., 2006) at various airmasses to provide both photometric and astrometric calibrations of the discovery images.

The images were pre-processed with standard techniques; the bias levels were removed, and a master bias frame, set as the average of 10 bias images was removed from all science frames. A master sky-flat was produced from the science frames using a clipped median filter, and was removed from the science images producing background variations no larger than  $\sim 1\%$  across a mosaic.

Photometric calibrations were done on a chip-by-chip basis using the Mega-pipe source catalog of the D1 and D4 fields (Gwyn, 2008). The zeropoint was found to be identical for all chips within uncertainties, with a value,  $Z_{r_{Subaru}} = 27.50 \pm 0.02$ . The conversion from the Suprime-cam instrumental magnitudes to those of Mega-pipe was found to be

$$m(r')_{Suprime} = m(r')_{Mega} - 0.018(g'_{Mega} - r'_{Mega}). \quad (1)$$

Atmospheric extinction was measured from the science frames. The airmass correction was found to be 0.08 magnitudes per unit increase in airmass. Comparison of common background sources in each triplet revealed no large seeing or transparency variations throughout the night (see Figures 2 and 3); the night was photometric.

The Suprime-cam field of view is highly distorted, especially near field edges, requiring calibration to ensure accurate astrometry of moving sources in the observations. Scamp (Bertin, 2006) was used to measure second order spatial distortions of the Suprime-cam field, from the D1 and D4 fields on a chip-by-chip basis. Little variance in the distortions was found over the airmass range of these observations. Thus, a master distortion map for each chip was produced from all images of the D1 and D4 fields. Absolute calibration of each science image was done using the USNO-B catalog, and the master distortion map, resulting in residuals of roughly 0.3". Relative astrometry between the three images of each field - a triplet - was performed by matching sources between an image, and the reference image, chosen as the image of the triplet with the lowest absolute residuals. This resulted in an excellent common astrometric solution for the triplet, with residuals of  $\lesssim 0.06''$  between all three images. This calibrations procedure ensured reliable astrometry to both maximize the discovery efficiency of moving sources, as well as secure the possibility of follow-up on future dates.

## 2.2. Moving Object Search

The Suprime-cam data were utilized to search for moving objects in the Solar system, in and beyond the orbits of the gas-giant planets. To characterize the detection efficiency of our moving object detection method, artificial moving point sources were implanted in the observations.

The stellar point-spread function (PSF) was generated on an image-by-image and chip-by-chip basis from 10-15 hand-selected, visually inspected point sources for each chip. It was found that a spatially constant PSF was sufficient to model the stellar shape across a chip. The PSFs were created using the tools in the *doaphot* package of *IRAF* and for each image consisted of an average Moffat profile with look-up table of the PSF stars of that chip.

Random artificial sources were generated on Sun-bound orbits, with semi-major axes,  $18 \leq a \leq 1000$  AU, eccentricities,  $e \leq 0.6$ , and inclinations,  $i \leq 90^\circ$ . Anomaly, periapse, and nodal angles were chosen at random to ensure that the sources fell in the images and could be either approaching or receding from their nodes. 20-30 artificial sources were planted in each chip with apparent magnitudes in the range  $21 \leq r' \leq 26.5$  with image-to-image flux variations matching those measured from 30-40 bright stars common to each image of a triplet, thus ensuring that any extinction variations throughout the observations were accounted for. If an artificial source's motion would cause it to drift more than 0.2 pixels during an exposure, it was broken up into multiple fainter sources with 0.2 pixel spacing and a total flux equal to that of the artificial source. Thus, trailing effects were fully accounted for in our search.

Moving objects were identified by their motions between images of a triplet. Using SExtractor (Bertin et al., 2002), all sources in an image were tabulated. Stationary sources common to each image in a triplet were flagged, and ignored from further consideration, leaving only those sources who were either moving, or had highly variable fluxes. The remaining sources of an image triplet were then searched for motion consistent with Sun-bound objects. Candidate sources were chosen as any three individual point-source detections, one per image, whose centroid moved at least one pixel (0.2") and at most  $\sim 5''$  between each image. These candidate sources were then further filtered by *fit\_radec* (Bernstein and Khushalani, 2000). If the best-fit orbit to the candidate had a chi-squared larger than 7.5, the candidate was rejected. The results of this were approximately 16000 candidate sources which were then visual inspected by an operator for final acceptance or rejection.

The majority of visually inspected candidates were false, primarily caused by cosmic ray impacts, or extended sources which were identified by SExtractor as more than one source in some images. Of the 16,000 candidates, roughly a third were matched with implanted artificial sources. From these sources, the performance of the search routine was characterized. The results are shown in Figure 4. As can be seen, the detection efficiency is well described by the familiar functional form

$$\eta(r') = \frac{A}{2} \left( 1 - \tanh \left( \frac{r' - m_*}{g} \right) \right) \quad (2)$$

where  $A$ ,  $m_*$ , and  $g$  are the maximum efficiency, half-maximum magnitude, and half-width parameters. The survey achieved a 50% limiting magnitude for discovery of  $r'=24.7$ . The search was found to be sensitive to objects as distant as  $\sim 900$  AU, beyond which, insufficient motion was exhibited for reliable detection. No significant variation in search efficiency with inclination or eccentricity was found (see Figures 5 and 6).

The search resulted in the detection of 88 sources. The sources' distances and inclinations were determined with *fit\_radec*. Photometry was measured using standard aperture photometry techniques with corrections for airmass applied (see Figure 3). Aperture corrections were measured from the bright stars from which the PSFs were generated. Photometric uncertainties were determined from the function

$$\Delta r' = \delta + \gamma 10^{\frac{r'-Z}{2.5}} \quad (3)$$

where  $\delta$  is a constant representing the extinction stability of the night in question,  $\gamma$  is a constant proportional to the parameters of the detector (see Fraser et al., 2008, for a derivation), and  $Z$  is the telescope photometric zeropoint. This function was fit to the difference in measured and planted magnitudes of the artificial sources. The best-fit parameters are  $(\delta, \gamma) = (0.028, 3.25)$ . The best-fit  $\delta$  is in agreement with the scatter in extinction exhibited in Figure 3. Along with the measured fluxes with uncertainties sampled per measurement from Equation 3, these results are presented in Table 2.

One detected object was identified as previously known Plutino 2004 VT75 which was not known to be in the observed fields prior to detection. This detection confirmed the accuracy of both the photometric and astrometric calibrations. The detected position of 2004 VT75 was  $\sim 0.2''$  from that predicted from the Minor Planet Center. As well, this source was detected across different chips demonstrating that the astrometric fits for different chips of the same mosaic image are reliable in an absolute sense.

### 2.3. Follow-up

For a subset of the objects, follow-up observations were performed with the Low Resolution Imaging Spectrometer (LRIS) on the Keck-I telescope on the nights of November 21st, 22nd and December 21st, 2009 (UT). LRIS is a dual channel (blue and red) camera, with each camera, a 2 CCD

mosaic having approximately a  $6 \times 8'$  field of view, with a  $\sim 25''$  gap, and a pixel scale of  $0.135''$ . This particular instrument is convenient for our follow-up observations, as the positional uncertainty ellipse of our targets at the time of follow-up was slightly smaller than the areal coverage of a single detector CCD.

The follow-up observations consisted of pairs of images at the positions of each target, predicted from *fit\_radec*, with temporal spacing between each image sufficient to detect the object's motion. By virtue of the dual channel imaging abilities of the camera, images in both the g and r LRIS filters were taken simultaneously. Exposure times were scaled from the flux of each source in the discovery images, and were chosen such that each source would have a photometric signal-to-noise ratio of  $\sim 10$  in each image. Images of the D1 and D4 Supernova fields were taken for calibration purposes.

Due to time constraints, only those objects whose distance might place them beyond 39 AU, and with magnitude in discovery images brightward of  $r' = 24.5$  were followed. 41 objects satisfied these constraints and were pursued in the follow-up observations.

Due to the geometry of the follow-up observations, asteroid confusion was a concern. The predicted rate of motion of the follow-up targets was used as a diagnostic of whether or not a detected moving object was the correct source. The second CCD of the LRIS detector provided a measure of this asteroid confusion rate, as no Kuiper belt objects were expected to fall within this region of the images. In the November follow-up data, 3 asteroids with brightnesses and rates of motion consistent with our Kuiper belt targets were found in the second CCD for all follow-up exposures. With the exception of two follow-up pointings, our objects were not confused, as only one moving target per field was identified with a rate of motion consistent with the targeted source. This is consistent with our asteroid confusion rate determined from the other CCD. Special attention for the two objects with confused follow-up was made during the December observations. From the December data, the interloper in the November observations was easily rejected achieving reliable links between the discovery and follow-up images for all follow-up targets. No confusion occurred during the December follow-up.

Our follow-up efforts were rewarded with 100% success rate for all 41 targets satisfying our dis-

tance and magnitude cuts. The conditions on the November nights were photometric and of moderate seeing, with full-width at half maximum  $\lesssim 1.5''$ . On the night in December, while it was photometric, the seeing conditions were mediocre, reducing the observing efficiency compared to the November nights. As such, all of the 41 objects for which we attempted follow-up have month-long arcs, while only a small subset of 10 have arcs longer than this. The results of the follow-up efforts are presented in Table 2.

Astrometric and photometric calibrations of the LRIS images were performed using the same techniques as applied to the Suprime-cam images. The astrometric distortions of the LRIS field were small, but noticeable, and varied with airmass. Distortion maps extracted from the calibration images at airmasses similar to the science images provided residual errors of  $\sim 0.3-0.4''$  with respect to the USNO-B catalog.

For the LRIS blue-channel, the photometric zero-point was found to be  $Z_{g_{Keck}} = 27.91 \pm 0.03$  with an airmass term  $A_g = 0.15 \pm 0.05$ . During the observations, the LRIS red-channel detectors were plagued by electronics difficulties causing charge transfer inefficiencies that were dependent on source flux. This effect was found to be as much as  $\sim 10\%$  in engineering images. As such, we adopt a 10% uncertainty on the zeropoint of this detector, and find,  $Z_{r_{Keck}} = 28.55 \pm 0.1$ . The red-airmass term was found to be  $A_r = 0.08 \pm 0.03$ .

The conversions between the LRIS r and g magnitudes and the r' and g' Mega-pipe magnitudes were found to be

$$m(r)_{Keck} = m(r'_{Mega}) - 0.2(g'_{Mega} - r'_{Mega}) \quad (4)$$

and

$$m(g)_{Keck} = m(g'_{Mega}) + 1.2(g'_{Mega} - r'_{Mega}). \quad (5)$$

The relatively large correction between  $g_{Keck}$  and  $g'_{Mega}$  is caused by the LRIS beam-splitter configuration which, in the configuration we utilized, truncated the red side of the  $g_{Keck}$  filter while preserving the throughput across the  $r_{Keck}$  filter.

#### 2.4. Color Conversion

To facilitate the combination of the discovery and follow-up images, all photometry needed to be

converted to a single system. The Sloan system (Smith et al., 2002) was chosen. The conversion from Megaprime magnitudes to the Sloan system are

$$r'_{Mega} = r'_{Sloan} - 0.024(g'_{Sloan} - r'_{Sloan}) \quad (6)$$

and

$$g'_{Mega} = g'_{Sloan} - 0.153(g'_{Sloan} - r'_{Sloan}). \quad (7)$$

From Equations 1, 4, and 5 and the conversions presented above, we find that the conversions from the Subaru and Keck photometry to the Sloan system are

$$r'_{Sloan} = r_{Keck} - 0.094(g_{Keck} - r_{Keck}), \quad (8)$$

$$g'_{Sloan} = g_{Keck} - 0.445(g_{Keck} - r_{Keck}), \quad (9)$$

and

$$r'_{Sloan} = r_{Subaru} - 0.019(g_{Keck} - r_{Keck}). \quad (10)$$

Using Equations 8-10, all photometry have been converted to the Sloan system. The photometry presented in Table 2 are the weighted averages of all measurements presented here. When no  $(g_{Keck} - r_{Keck})$  colour was available, the average color of all those objects that did receive follow-up,  $(g_{Keck} - r_{Keck}) = 1.21$  was used to convert to the Sloan survey. As the range of Keck colors for our sample is  $0.68 \leq (g_{Keck} - r_{Keck}) \leq 1.96$ , we estimate the error in the conversion caused by using this average color is  $\sim 0.02$  magnitudes, negligibly small.

In Figure 7 we present the  $(g'_{Sloan} - r'_{Sloan})$  color versus inclination for those objects with follow-up observations. From this figure, it can be seen that our sample exhibits similar behaviour to the Kuiper belt objects in the Minor Planet Center analyzed by Peixinho et al. (2008). That is, there is a correlation with colour and inclination; low inclination objects are typically redder than higher inclination objects. As both our colours and inclinations are significantly more inaccurate than those in the sample analyzed by Peixinho et al. (2008), a repeat of the same analysis on our data is not warranted, as no more insight would be gained than by visually comparing our sample to theirs (see Figure 1 of Peixinho et al. (2008)).

### 3. Analysis

As found by Bernstein et al. (2004), there seems to be some variation in the Kuiper belt size distribution with orbital excitation. More specifically, they defined two populations, the *Cold* sample, which contains those objects with heliocentric distances,  $38 < d < 55$  AU and inclinations,  $i < 5^\circ$ , and the *Excited* population as all those Kuiper belt objects in the same distance range, but with large inclinations. Bernstein et al. (2004) found that for bright objects ( $R < 24$ ), the *Cold* population had a much steeper size distribution than the *Excited* population. This result was found from a sample of Kuiper belt objects compiled from a large number of different surveys, providing a result possibly affected by calibration errors and sky density variations.

Elliot et al. (2005) analyzed the results of the Deep Ecliptic Survey, and found similar results. That is, that the cold classical objects have a steeper size distribution than the resonant, or excited populations. This result however, was drawn from a survey without a calibrated detection efficiency, making the result untrustworthy.

Fuentes and Holman (2008) performed a similar analysis as Bernstein et al. (2004), but with additional survey data. Their findings were similar, i.e., that the hot population size distribution is shallower than that of the cold population. But much like Bernstein et al. (2004), they considered data from multiple surveys and may have been affected by the same calibration errors and sky density variations.

Fraser et al. (2008); Fraser and Kavelaars (2009) reanalyzed the survey data considered in Bernstein et al. (2004) along with new observations, and introduced a technique which accounted for possible errors induced from combining the results of different surveys when measuring the size distribution. They found that the apparent differences between the hot and cold populations could not be disentangled from possible effects caused by the combination of different surveys. When correctly accounting for these effects, no statistical difference between the hot and cold population was found. Population differences as large as those inferred by Bernstein et al. (2004) might exist, but their presence could not be discerned from the available data sets.

The survey we present here, has sufficient depth, and number of detections to probe the differences in size distributions of the hot and cold populations

alone, without the need for other data. By doing so, we can ensure that the biases that may be introduced from the use of multiple datasets are avoided here providing a clean and reliable test for any differences between the hot and cold populations of the Kuiper belt.

#### 3.1. The Samples

We want to test the findings of Bernstein et al. (2004). To that end, we define subsets of our detections, which are similar to those considered by Bernstein et al. (2004). They are defined as follows:

1. We define *TNO* sample, as all the detections in our sample.
2. Like Bernstein et al. (2004) we define the *Cold* population as those objects with  $38 < d < 55$  AU and  $i < 5^\circ$ . We also further refine this, and define the *Cold<sub>F</sub>* sample as only those sources from the *Cold* sample who received follow-up observations in addition to the discovery observations.
3. We define the *Hot<sub>F</sub>* and *Hot* samples as those objects with  $38 < d < 55$  AU and  $i > 5^\circ$ , who have and have not received follow-up observations respectively.
4. We define the *Close* population, as those objects with  $30 < d < 38$ . We do not make any distinction about follow-up, as the majority of the *Close* population was not observed beyond the discovery observations.

We note here that the exact inclination division between the *Cold* and *Hot* populations is uncertain. Measurements of the inclination distributions of the *Hot* and *Cold* samples suggest that the vast majority of cold classical objects will have inclinations less than  $i \sim 5^\circ$  (Brown, 2001; Gulbis et al., 2010). Analysis of the optical colour distribution of Kuiper belt objects reveals a correlation of colour with inclination (Peixinho et al., 2008, for a recent example, see) that suggests there is a division between low-inclination red objects, and low-inclination neutral objects at  $i \sim 12^\circ$ . Given the uncertainty of the inclination division that separates the *Cold* and *Hot* populations, we consider the full range of inclination divisions testable by our observations and primarily discuss the historical division of  $i = 5^\circ$  unless otherwise stated.

The *Close* population is a mix of objects in mean-motion resonances with Neptune, the Centaurs, and the scattered disk objects. On the other hand,

the *Hot* population consists of hot classical, resonant, and scattered disk objects. While the exact fractional mix of each of these populations cannot be determined from our observations, the Minor Planet Center can guide us as to which populations dominate these subsamples. Analysis of the objects in the Minor Planet Center, near opposition in late October, within a few degrees of the ecliptic, reveals 13 objects satisfying  $30 < d < 38$  AU, 6 of which are Plutinos, and 36 objects satisfying  $d > 38$  AU and  $i > 5^\circ$ , of which only a few are Plutinos, with the majority being hot classical and scattered disk objects. As the relative mixes of each dynamical class are different for the *Hot* and *Close* subsamples, any differences detected in the size distributions of the subsamples can provide insight into the size distributions of the underlying populations.

### 3.2. The Methods

As the Kuiper belt objects we detect are not resolved, we have no measure of their sizes, and therefore cannot measure the size distribution of our sample directly. Rather, we must use an indirect technique, and infer the size distribution from the luminosity function. Brightward of  $R \sim 25$ , the luminosity function is well represented by a power-law. That is, the differential surface density of objects with magnitude  $m$  per square-degree is given by

$$\Sigma(m) = \alpha \ln(10) 10^{\alpha(m-m_o)} \quad (11)$$

where  $\alpha$  is the logarithmic slope of the power-law, and  $m_o$  is the magnitude at which there is one object per square degree with that magnitude, or brighter. Recent measurements suggest that, for the *TNO* sample,  $\alpha = 0.73 - 0.76$  and  $m_o \sim 23.4$  in the R-band (Fuentes et al., 2009; Fraser and Kavelaars, 2009). It is worth noting that the luminosity function has a break, or transition from the steep slope for large objects, to a shallower distribution for fainter sources. The transition occurs around  $R \sim 25$ , which is at the tail end of our survey sensitivity. As such, the break will have little to no effect on our observations, and we ignore it in our analysis.

It can be shown that if the size distribution of a population is a power-law, with slope  $q$ , i.e.,  $\frac{dN}{dr} \propto r^{-q}$ , then the luminosity function of that population is given by Equation 11, with slope  $\alpha = \frac{q-1}{5}$ . As such, the slopes of the size distributions of each

population can be determined from their luminosity functions (see Fraser et al., 2008, for a thorough discussion of this technique).

The fits of Equation 11 is done with a Bayesian maximum likelihood technique. Specifically, the likelihood

$$L(\{m\} | \alpha, m_o) = e^{-\Omega \int \eta(m) \Sigma(m | \alpha, m_o) dm} \times \prod_i \sigma(m_i) \Sigma(m_i | \alpha, m_o) \quad (12)$$

is maximized over the luminosity function slope and normalization parameters,  $\alpha$  and  $m_o$ . Here  $\Omega$  is the areal coverage of our survey,  $\{m\}$  is the set of magnitudes for our discovered objects, with  $m_i$  the magnitude of object  $i$ .  $\sigma(m_i)$  is a functional representation of the uncertainty in the magnitude  $m_i$ . As standard practice, we adopt a gaussian representation, with widths equal to the uncertainty in the observed magnitude of each source.

To avoid potential errors induced at low detection efficiencies, we consider only those sources with probability of detection greater than 50% and truncate our detection efficiency below this point. Fraser et al. (2008) has demonstrated that truncating the efficiency at 50% as we do here causes the best-fit slope  $\alpha$  to appear roughly 3-5% steeper than in reality. This effect however, is much smaller than the uncertainty in the best-fit slopes we present. For the *Cold<sub>F</sub>* and *Hot<sub>F</sub>* samples, our follow-up is limited to those sources with  $r'_{Subaru} < 24.5$ . Thus  $r' = 24.5$  is our magnitude cut for the *Cold<sub>F</sub>* and *Hot<sub>F</sub>* samples. In Equation 11 we utilize only the magnitudes from discovery observations alone, as utilizing the data from other filters could possibly introduce biases into the results. We note however, that when utilizing all available flux measurements, the change in the results was significantly smaller than the uncertainties in the best-fit parameters.

To test the quality of the best-fits, we utilize the Anderson-Darling statistic,

$$\Delta = \int_0^1 \frac{(S(m) - P(m))^2}{P(m)(1 - P(m))} dP(m) \quad (13)$$

where  $P(m)$  is the cumulative probability of detecting an object with magnitude  $\leq m$ , and  $S(m)$  is the cumulative distribution of detections. We calculate the probability,  $P(\Delta > \Delta_{obs})$  of finding a value,  $\Delta$ , larger than that of the observations,  $\Delta_{obs}$ , given the

best fit-parameters by bootstrapping the statistic, i.e., randomly drawing a subsample of objects from the best-fit power-law, with number equal to that detected in a particular sample, fitting Equation 11 to that random sample, and computing  $\Delta$ . Values of  $P(\Delta > \Delta_{obs})$  near 0 indicate that the functional form is a poor representation of the data.

### 3.3. The Results

The luminosity functions of the *TNO*, *Cold*, *Hot*, and *Close* samples are presented in Figure 8. The results of the fits of Equation 11 to the various subsamples are shown in Figure 9, and Table 3.

As can be seen from Figures 8 and 9, the *Cold<sub>F</sub>* exhibits a much steeper luminosity function, with slope  $\alpha_{Cold} = 0.82 \pm 0.23$  than the *Hot<sub>F</sub>* population which has slope  $\alpha_{Hot} = 0.35 \pm 0.21$ . The slopes of these two populations differ at more than the  $1\text{-}\sigma$  level. Both of these samples are well described by power-laws, as exhibited by their Anderson-Darling statistics (see Table 3). Similar slopes within the uncertainties are found from the *Hot* and *Cold* samples. But these values are less trustworthy as the inaccurate inclinations of those objects which did not receive follow-up cause an uncertain amount of mixing between the two subsamples.

In addition, the *Close* sample exhibits virtually the same luminosity function slope,  $\alpha_{Close} = 0.40 \pm 0.15$  as the *Hot<sub>F</sub>* ( and *Hot* ) sample. As the *Close* and *Hot* subsamples are made up of different fractions of the Centaur, resonant, hot classical, and scattered populations, these results suggests that all of these populations exhibit equally shallow luminosity functions. If one or more of the populations had a luminosity function as steep as the *Cold* population, it would likely be detectable as a difference in  $\alpha$  between the *Hot* and *Close* populations, the steeper being the subsample with the greatest fraction of the steep dynamical population. This however, is not apparent. Indeed, the slope does not change when considering the *Hot* and *Close* populations together, resulting in  $\alpha_{Hot+Close} = 0.40 \pm 0.12$ .

The luminosity function of *TNO* sample has a slope  $\alpha_{TNO} = 0.56 \pm 0.1$ , which is significantly shallower than the slope  $\alpha \sim 0.75$  found from other recent measurements in the same magnitude range (Fuentes et al., 2009; Fraser and Kavelaars, 2009). This surprising result can be understood relatively simply. The *TNO* sample, is a mixture of the *Hot*, and *Cold* populations, which our results have shown

have significantly different slopes. As such, we expect the *TNO* sample to have a slope bounded by the slopes of the *Hot* ( $\alpha_{Hot} \sim 0.4$ ) and *Cold* ( $\alpha_{Cold} \sim 0.8$ ) populations. Our observations were made at a ecliptic longitude where plutinos, which are primarily members of the hot population, are preferentially at perihelion (see above). As such, we expect a greater fraction of Plutinos detected in our observations, than at other longitudes where Plutinos are not at perihelion. As the *Hot* population has a shallower luminosity function than the *Cold* population, we expect to see a flatter luminosity function for the *TNO* sample at this longitude than at others. This simple reasoning can account for the variation in luminosity function slopes seen in past surveys (see Fraser et al., 2008).

Along with the size distribution differences between the *Hot* and *Cold* populations, the colour distribution (Tegler and Romanishin, 2000; Trujillo and Brown, 2002; Peixinho et al., 2008, and see Figure 7), inclination distribution (Brown, 2001), binary fraction (Stephens and Noll, 2006) and lack of large objects on dynamically cold orbits (Brown, 2008) suggest that these two populations are different. There is no clear evidence however, for a clean separation in inclination between the two. Rather, it is more likely that a smooth gradient exists, and as such, the historical division of  $i_{div} = 5^\circ$  chosen to separate these two populations is relatively arbitrary. As such, we measured the luminosity function slopes while varying  $i_{div}$ . The results are presented in Figure 10.

As can be seen, the *Cold* and *Hot* population slopes become significantly different for  $i_{div} \gtrsim 5^\circ$ . When considering all objects, not just those with follow-up, the slope of the *Hot* population seems to become a constant, with  $\alpha_{Hot} \sim 0.4$  for  $i_{div} \geq 6^\circ$ . This suggests that above  $6^\circ$  the fraction of the population with a steep size distribution is insignificant, and the observed objects come almost entirely from the population with a shallow size distribution. As the uncertainty on  $\alpha$  is still quite large, these observations however, are insufficient to confirm such a hypothesis.

To test the significance of the apparent difference in luminosity functions of the *Hot* and *Cold* populations, we utilize two different statistical tests. We first utilize the Kuiper-variant of the Kolmogorov-Smirnov test as a non-parametric measure of the significance in the observed difference between two populations (Press, 2002). We randomly bootstrapped from the cumulative luminosity function



of the *Cold* sample, a sample of objects equal in number to the *Hot* sample. We then calculated the KS-statistic of this random sample compared to the *Cold* sample. This process was repeated, and from this the probability of finding a simulated KS-statistic as large or larger than that found from the actual *Hot* population was determined. We found that the two populations were drawn from separate parent populations at the 80-90% significance levels for inclination divisions  $i_{div} \geq 4^\circ$ .

While the KS-test provides a non-parametric test, a better measure of the significance difference of the *Hot* and *Cold* populations can be found with the knowledge that the two populations are well described by power-laws. To that end, we also utilized the Anderson-Darling statistic, as done in Bernstein et al. (2004); Fraser et al. (2008). Following similar procedures as above, by randomly sampling from the best-fit power-law of the  $Cold_F$  sample we determined the probability of finding a simulated Anderson-Darling statistic as large or larger than that found from the actual  $Hot_F$  population as compared to the observed  $Cold_F$  sample. We found that the two populations were drawn from separate parent populations at greater than the  $3\text{-}\sigma$  significance for inclination divisions  $i_{div} \geq 4^\circ$ .

## 4. Discussion

### 4.1. Implications for the Kuiper belt

The observed luminosity functions imply size distribution slopes  $q_{Cold} = 5.1 \pm 1.1$ ,  $q_{Hot} = 2.8 \pm 1.0$ , and  $q_{Close} = 3.0 \pm 0.8$  for the *Cold*, *Hot*, and *Close* populations. The consistency of the *Hot* and *Close* populations leaves us to consider the two populations together, implying a slope for the combined population of  $q_{Hot+Close} = 3.0 \pm 0.6$ .

Though the results presented by Bernstein et al. (2004) and Fuentes and Holman (2008) were possibly affected by sky density variations and calibration errors, we find similar conclusions, ie., the *Cold* population size distribution is steeper than the *Hot* population size distribution. Given the similarity in these repeated measurements of the Kuiper belt luminosity function, the results stand confident.

While over the magnitude range of our observations, both the *Hot* and *Cold* populations are well described by power-law models, other works have put into question whether the power-law behaviour extends to all brightnesses. The fact that

the luminosity function of the *TNO* population exhibits a roll-over at magnitudes  $R \gtrsim 25$  is well accepted. The results of Bernstein et al. (2004) however, suggest that the power-law behaviour of the *Cold* population breaks down for the brightest objects. Specifically they find that at the bright-end, the *Cold* population luminosity function has a steeper slope than at fainter magnitudes. Similarly, Morbidelli et al. (2009) suggests that the *Hot* and *Cold* populations are intimate mixtures of two primordial populations, one with a steep size distribution, and one with a shallow size distribution. In such a scenario, both populations should exhibit shallow slopes for the largest objects, then turn-up to a steeper slope for smaller objects, before finally breaking to a shallow slope at some size where collisional processing has dominated. To that end, we test the power-law behaviour of both the *Hot* and *Cold* populations.

For the *Cold* population, a simple extrapolation of the best-fit luminosity function suggests that the brightest object on the sky in this population should have a magnitude of  $R \sim 19.5$ . The entire low-latitude Kuiper belt has been surveyed for objects to a limiting magnitude of  $R \lesssim 21$  (Trujillo and Brown, 2003), and the brightest known *Cold* object has  $R \sim 21.3$ , nearly a full magnitude fainter. This observation confirms the results of Bernstein et al. (2004). Namely, that the power-law behaviour of the *Cold* population luminosity function cannot extend to the brightest targets. Rather the power-law must be truncated. The exact behaviour cannot be determined from the observations we present here. The suggestion by Morbidelli et al. (2009) that the cold population size distribution will have a shallow slope for the largest objects, and a turn-up to the observed steep is excluded by this result.

Similarly, extrapolating the best-fit power-law luminosity function of the *Hot* population suggests that this population is well described by a power-law to its brightest objects. Indeed, when excluding the largest objects which are known to have different albedos than the objects observed here (Stansberry et al., 2008) the absolute magnitude distribution of the biggest objects has a slope compatible with our observations (Brown, 2008; Morbidelli et al., 2008). To test the exactness of a power-law requires combination of other survey data sensitive to the brightest *Hot* members. As well this analysis should include modelling of the latitude distribution of the *Hot* population. The

fact however, remains that the *Hot* population has a flat size distribution over all observable sizes.

The behaviour of the *Hot* population luminosity function at the faint end is uncertain; the shallow slope of  $\alpha_{Hot} \sim 0.35$  for  $R \lesssim 25$  is compatible with the lack of faint detections of the *Hot* population in fainter surveys, eliminating the need for a break at the faint end. If however, the *Hot* population slope is as steep as the upper limits of our confidence interval, a break at magnitudes fainter than  $R \sim 26$  is still required. The existence of a break in the *Hot* population will only be confirmed by an off-ecliptic survey sensitive to objects with  $R > 26$ .

The turn-up, as proposed by Morbidelli et al. (2009) would produce an abundance of faint objects in our observed *Hot* population. We can test this utilizing the Anderson-Darling statistic. We generate a fake *Hot* subsample from a shallow power-law with the observed *Hot* population slope that turns up to the best-fit observed slope of the *Cold* population,  $\alpha_{Cold} = 0.8$ , at some magnitude  $m_{TU}$ . We then fit a power-law to that sample, and calculate the Anderson-Darling statistic. This is repeated, and the probability of finding a statistic worse than the observations is calculated versus the value of  $m_{TU}$ . The strength of this test is weakened by the sparse sampling of high-latitude sources in our dataset. We still however, eliminate such a turn-up to the slope of the *Cold* population for  $m_{TU} < 24.2$  ( $r'$ ) at the  $2\text{-}\sigma$  level and  $< 23.6$  at the  $3\text{-}\sigma$  level. This is incompatible with the assertion of Morbidelli et al. (2009) who suggest that the *Hot* population should have the same slope as the *Cold* population over an absolute magnitude range of  $6.5 < H < 9$ , corresponding to  $r'$  magnitudes,  $22 \lesssim r' \lesssim 24.5$ . The significance of the test results over the entire magnitude range however, prevents this result from being iron clad. Clearly, the possibility of a turn-up (or down) must be tested from a survey which detects a large sample of high-latitude objects.

The difference in size distribution slopes of the *Hot* and *Cold* populations suggest very different histories for these two groups. Interestingly, the shallow slope of the *Hot* distribution is compatible with a heavily collisionally processed population, either one that has reached collisional equilibrium, or in which the largest objects are fragments of even larger, disrupted primordial bodies (O'Brien and Greenberg, 2003; Bottke et al., 2010). For collisional evolution to completely reshape the size distribution of the *Hot* population

would require extremely high collision rates, seemingly incompatible with plausible protoplanetary disk densities, and formation scenarios (Stern, 1996; Kenyon and Bromley, 2004; Fraser, 2009). Rather it is likely that this slope is the result of the accretionary processes that formed the *Hot* population.

Unlike the *Hot* population, the steep slope of the *Cold* population is entirely incompatible with a collisionally evolved distribution. This slope must be the result of accretionary processes as well.

The shallower slope of the *Hot* population, and the fact that the largest objects of the *Hot* population are larger than those of the *Cold* population, implies that the *Hot* population achieved a more advanced stage of accretion than the *Cold* population (Kenyon, 2002). The incompatibility of their slopes implies that these two populations underwent different accretion scenarios. It is possible, that the *Hot* population underwent a longer duration of accretion than the *Cold* population. To halt accretion for the *Cold* population would require excitation and mass depletion with some yet unseen perturber beyond the outer edge of the Kuiper belt. The past existence of one or more planetary embryos in the Kuiper belt region is a possible source of this excitation, and has been proposed to explain some of the Kuiper belt dynamical features (Gladman and Chan, 2006; Lykawka and Mukai, 2008).

Another possibility is that the *Hot* population underwent accretion in a more dense region of the protoplanetary nebula. This would result in more rapid accretion than compared to the *Cold* population, allowing the *Hot* population to grow to larger sizes before the process was halted. Under this scenario, the *Hot* and *Cold* populations could then have similar accretion timescales. As currently favoured formation scenarios suggest the *Hot* population was scattered from a region closer to the Sun than their current locations (Malhotra, 1993; Gomes, 2003; Levison et al., 2008), where the protoplanetary disk might have been more dense, this scenario seems likely.

However the *Hot* and *Cold* populations came about, their incompatible size distributions imply different accretion scenarios. Once accretion was finished, these objects were excited and emplaced onto their current orbits, creating the architecture of the current Kuiper belt. Given the dynamically cold nature of the *Cold* population, it seems plausible that this population formed in-situ. What ever the mechanism(s) ultimately responsible for

the belt, our results show that little mixing between the *Hot* and *Cold* populations has occurred.

#### 4.2. Comparison with Other Populations

There is a striking similarity in the size distributions of the *Cold* population, and the Jupiter Trojans. Both have similarly steep slopes, ( $q_{Cold} \sim 5.1$  and  $q_{JT} \sim 5.5$ ), and both exhibit breaks to shallower slopes at roughly the same object diameter (Jewitt et al., 2000; Fraser and Kavelaars, 2009). This result argues strongly against the Trojan formation mechanism of the so-called NICE model in which the Trojan populations and the hot and cold Kuiper belt populations are all scattered into their current regions from the same primordial disk population (Morbidelli et al., 2005; Nesvorný and Vokrouhlický, 2009). If this scenario were true, Morbidelli et al. (2009) has shown that over the magnitude range of our observations, the hot population should have the same slope as that observed for large Jupiter trojans. Using the Anderson-Darling statistic, we tested the probability of the *Hot* sample being drawn from a luminosity function with the slope of the Jupiter trojan luminosity function,  $\alpha_{JT} = 0.9$ . We found that the *Hot* sample could not be drawn from the Jupiter trojan population at greater than the  $3\text{-}\sigma$  significance. As the size distributions of these two populations in the size range considered have not evolved significantly since they were emplaced in their current regions (Davis et al., 2002; Fraser and Kavelaars, 2009), we must conclude that the hot and Jupiter trojan populations must have different progenator populations. This result and the lack of mixing between the hot and cold populations is difficult to reconcile with the NICE model. It seems likely the hot, cold, and trojan populations formed by separate means. If this is true, the similarities between the cold and trojan populations are quite a coincidence.

Another similarity is seen between the *Hot* population ( $q_{Hot} \sim 3$ ) and the Jupiter family comets, who exhibit a size distribution slope of  $q_{JFC} \sim 2.8$  albeit over a smaller size range,  $1 \lesssim D \lesssim 10$  km (Tancredi et al., 2006; Weissman et al., 2009). This resemblance is interesting as one likely source of Jupiter family comets are scattered disk objects - members of the *Hot* population - which have fallen into the inner Solar system under gravitational perturbations from the gas-giants, suggesting that the scattered disk size distribution might be a power-

law for  $D \gtrsim 1$  km. We consider this possibility here.

While the observations we present do not measure the size distribution of the scattered disk directly, the similarity in slopes between the *Hot* and *Close* subsamples implies that the scattered disk cannot have a size distribution significantly different than that of the *Hot* sample as a whole. Additionally we cannot determine the total number scattered disk objects from our observations. Rather, we turn to other estimates which suggest that, if their size distribution is a power-law with slope of  $q \sim 3$ , then there are roughly  $10^7 - 10^8$  scattered disk objects with  $1 \lesssim D \lesssim 10$  km (Trujillo et al., 2000; Parker and Kavelaars, 2010, Schwamb, personal communication).

Simulations by Volk and Malhotra (2008) suggest that if the scattered disk is the sole source of the Jupiter family comets, then there must be at least  $10^9$  objects in that population to account for the current flux of Jupiter family comets through the inner Solar system, implying that either the scattered disk is not the sole source of the Jupiter family comets, or that the extrapolation of a power-law to  $D \sim 1$  km is unreasonable; it must be that the size distribution of scattered disk objects steepens significantly in the  $D \sim 10 - 100$  km range. Further observations are required before this feature can be detected.

## 5. Conclusions

We have performed an ecliptic survey, and have detected 88 Kuiper belt objects with magnitudes  $21 < r'_{Sloan} < 25.2$ . A subset of these objects have received additional follow-up observations allowing us to accurately determine their inclinations and distances. Using these data, we have measured the size distribution of the *Hot* and *Cold* subsamples, historically defined as those objects with inclinations above and below  $5^\circ$  respectively. This measurement, which is independent of any previous observations has confirmed that the *Cold* population has a much steeper luminosity function, with slope  $\alpha_{Cold} = 0.82 \pm 0.23$ , than the *Hot* population, with slope  $\alpha_{Hot} = 0.35 \pm 0.21$ .

The observed luminosity functions imply different size distributions for the *Hot* and *Cold* populations. The size distribution slopes of the the two subsamples are  $q_{Cold} = 5.1 \pm 1.1$  and  $q_{Hot} = 2.8 \pm 1.0$ .

In addition, we have found that the *Close* population, which is defined as those objects with heliocentric distance,  $d < 38$  have the same luminosity function slope as the *Hot* subsample, demonstrating that these two share a similar size distribution. In addition, our findings suggest that the dynamical populations which make up both the *Hot* and *Close* populations must all have similar size distributions.

The primary consequence of these findings is that the *Cold* population, which consists primarily of cold classical Kuiper belt objects, has a separate, and distinct accretion history from the *Hot* population, requiring either potentially different accretion timescales for the two populations, or formation in different locations of the protoplanetary disk. These observations reveal the similarities in the size distributions between the subsamples of the Kuiper belt and the Jupiter family comets and Trojans, suggesting a connection between the formation and subsequent evolution of the small body populations of the outer Solar system.

## 6. Acknowledgements

Based in part on data collected at Subaru Telescope, which is operated by the National Astronomical Observatory of Japan. Some of the data presented herein were obtained at the W. M. Keck Observatory, which is operated as a scientific partnership among the California Institute of Technology, the University of California, and the National Aeronautics and Space Administration. This research used the facilities of the Canadian Astronomy Data Centre operated by the National Research Council of Canada with the support of the Canadian Space Agency. The research upon which this paper is based was supported by National Aeronautic and Space Administration (NASA) Grant No. NASA.000261

## References

Astier, P., Guy, J., Regnault, N., Pain, R., Aubourg, E., Balam, D., Basa, S., Carlberg, R. G., Fabbro, S., Fouchez, D., Hook, I. M., Howell, D. A., Lafoux, H., Neill, J. D., Palanque-Delabrouille, N., Perrett, K., Pritchet, C. J., Rich, J., Sullivan, M., Taillet, R., Aldering, G., Antilogus, P., Arsenijevic, V., Balland, C., Baumont, S., Bronder, J., Courtois, H., Ellis, R. S., Filiol, M., Gonçalves, A. C., Goobar, A., Guide, D., Hardin, D., Lusset, V., Lidman, C., McMahon, R., Mouchet, M., Mourao, A., Perlmutter, S., Ripoche, P., Tao, C., Walton, N., Feb. 2006. The Supernova Legacy Survey: measurement of  $\Omega_M$ ,  $\Omega_\Lambda$  and  $w$  from the first year data set. *A&A* 447, 31–48.

Benavidez, P. G., Campo Bagatin, A., Feb. 2009. Collisional evolution of Trans-Neptunian populations: Effects of fragmentation physics and estimates of the abundances of gravitational aggregates. *PSS57*, 201–215.

Bernstein, G., Khushalani, B., Dec. 2000. Orbit Fitting and Uncertainties for Kuiper Belt Objects. *AJ* 120, 3323–3332.

Bernstein, G. M., Trilling, D. E., Allen, R. L., Brown, M. E., Holman, M., Malhotra, R., Sep. 2004. The Size Distribution of Trans-Neptunian Bodies. *AJ* 128, 1364–1390.

Bertin, E., Jul. 2006. Automatic Astrometric and Photometric Calibration with SCAMP. In: C. Gabriel, C. Arviset, D. Ponz, & S. Enrique (Ed.), *Astronomical Data Analysis Software and Systems XV*. Vol. 351 of *Astronomical Society of the Pacific Conference Series*. pp. 112–+.

Bertin, E., Mellier, Y., Radovich, M., Missonnier, G., Dideolon, P., Morin, B., 2002. The TERAPIX Pipeline. In: Bohlender, D. A., Durand, D., Handley, T. H. (Eds.), *Astronomical Data Analysis Software and Systems XI*. Vol. 281 of *Astronomical Society of the Pacific Conference Series*. pp. 228–+.

Bottke, W. F., Durda, D. D., Nesvorný, D., Jedicke, R., Morbidelli, A., Vokrouhlický, D., Levison, H. F., Dec. 2005. Linking the collisional history of the main asteroid belt to its dynamical excitation and depletion. *Icarus* 179, 63–94.

Bottke, W. F., Nesvorný, D., Vokrouhlický, D., Morbidelli, A., Mar. 2010. The Irregular Satellites: The Most Collisionally Evolved Populations in the Solar System. *AJ* 139, 994–1014.

Brown, M. E., May 2001. The Inclination Distribution of the Kuiper Belt. *AJ* 121, 2804–2814.

Brown, M. E., 2008. The Largest Kuiper Belt Objects. pp. 335–344.

Davis, D. R., Durda, D. D., Marzari, F., Campo Bagatin, A., Gil-Hutton, R., 2002. Collisional Evolution of Small-Body Populations. *Asteroids III*, 545–558.

Elliot, J. L., Kern, S. D., Clancy, K. B., Gulbis, A. A. S., Millis, R. L., Buie, M. W., Wasserman, L. H., Chiang, E. I., Jordan, A. B., Trilling, D. E., Meech, K. J., Feb. 2005. The Deep Ecliptic Survey: A Search for Kuiper Belt Objects and Centaurs. II. Dynamical Classification, the Kuiper Belt Plane, and the Core Population. *AJ* 129, 1117–1162.

Fraser, W. C., Nov. 2009. The Collisional Divot in the Kuiper Belt Size Distribution. *ApJ* 706, 119–129.

Fraser, W. C., Kavelaars, J. J., Jan. 2009. The Size Distribution of Kuiper Belt Objects for  $D_{\text{gsim}} > 10$  km. *AJ* 137, 72–82.

Fraser, W. C., Kavelaars, J. J., Holman, M. J., Pritchet, C. J., Gladman, B. J., Grav, T., Jones, R. L., Macwilliams, J., Petit, J.-M., Jun. 2008. The Kuiper belt luminosity function from  $m_R = 21$  to 26. *Icarus* 195, 827–843.

Fuentes, C. I., George, M. R., Holman, M. J., May 2009. A Subaru Pencil-Beam Search for  $m_R \sim 27$  Trans-Neptunian Bodies. *ApJ* 696, 91–95.

Fuentes, C. I., Holman, M. J., Jul. 2008. a SUBARU Archival Search for Faint Trans-Neptunian Objects. *AJ* 136, 83–97.

Gladman, B., Chan, C., Jun. 2006. Production of the Extended Scattered Disk by Rogue Planets. *ApJL* 643, L135–L138.

Gladman, B., Kavelaars, J. J., Petit, J.-M., Morbidelli, A., Holman, M. J., Loredó, T., Aug. 2001. The Structure of the Kuiper Belt: Size Distribution and Radial Extent. *AJ* 122, 1051–1066.

Gomes, R. S., Feb. 2003. The origin of the Kuiper Belt high-inclination population. *Icarus* 161, 404–418.

- Gulbis, A. A. S., Elliot, J. L., Adams, E. R., Benecchi, S. D., Buie, M. W., Trilling, D. E., Wasserman, L. H., Aug. 2010. Unbiased Inclination Distributions for Objects in the Kuiper Belt. *AJ*140, 350–369.
- Gwyn, S. D. J., Feb. 2008. MegaPipe: The MegaCam Image Stacking Pipeline at the Canadian Astronomical Data Centre. *PASP*120, 212–223.
- Jedicke, R., Metcalfe, T. S., Feb. 1998. The Orbital and Absolute Magnitude Distributions of Main Belt Asteroids. *Icarus* 131, 245–260.
- Jewitt, D. C., Sheppard, S. S., Apr. 2002. Physical Properties of Trans-Neptunian Object (20000) Varuna. *AJ*123, 2110–2120.
- Jewitt, D. C., Trujillo, C. A., Luu, J. X., Aug. 2000. Population and Size Distribution of Small Jovian Trojan Asteroids. *AJ*120, 1140–1147.
- Kenyon, S. J., Mar. 2002. Planet Formation in the Outer Solar System. *PASP* 114, 265–283.
- Kenyon, S. J., Bromley, B. C., Oct. 2004. The Size Distribution of Kuiper Belt Objects. *AJ* 128, 1916–1926.
- Kenyon, S. J., Luu, J. X., May 1998. Accretion in the Early Kuiper Belt. I. Coagulation and Velocity Evolution. *AJ*115, 2136–2160.
- Levison, H. F., Morbidelli, A., Vanlaerhoven, C., Gomes, R., Tsiganis, K., Jul. 2008. Origin of the structure of the Kuiper belt during a dynamical instability in the orbits of Uranus and Neptune. *Icarus* 196, 258–273.
- Levison, H. F., Stern, S. A., Mar. 2001. On the Size Dependence of the Inclination Distribution of the Main Kuiper Belt. *AJ*121, 1730–1735.
- Lykawka, P. S., Mukai, T., Apr. 2008. An Outer Planet Beyond Pluto and the Origin of the Trans-Neptunian Belt Architecture. *AJ*135, 1161–1200.
- Malhotra, R., Oct. 1993. The Origin of Pluto's Peculiar Orbit. *Nature*365, 819–+.
- Miyazaki, S., Komiyama, Y., Sekiguchi, M., Okamura, S., Doi, M., Furusawa, H., Hamabe, M., Imi, K., Kimura, M., Nakata, F., Okada, N., Ouchi, M., Shimasaku, K., Yagi, M., Yasuda, N., Dec. 2002. Subaru Prime Focus Camera – Suprime-Cam. *pasj*54, 833–853.
- Morbidelli, A., Levison, H. F., Bottke, W. F., Dones, L., Nesvorný, D., Jul. 2009. Considerations on the magnitude distributions of the Kuiper belt and of the Jupiter Trojans. *Icarus* 202, 310–315.
- Morbidelli, A., Levison, H. F., Gomes, R., 2008. The Dynamical Structure of the Kuiper Belt and Its Primordial Origin. *The Solar System Beyond Neptune*, pp. 275–292.
- Morbidelli, A., Levison, H. F., Tsiganis, K., Gomes, R., May 2005. Chaotic capture of Jupiter's Trojan asteroids in the early Solar System. *Nature*435, 462–465.
- Nesvorný, D., Vokrouhlický, D., Jun. 2009. Chaotic Capture of Neptune Trojans. *AJ*137, 5003–5011.
- O'Brien, D. P., Greenberg, R., Aug. 2003. Steady-state size distributions for collisional populations: analytical solution with size-dependent strength. *Icarus* 164, 334–345.
- Parker, A. H., Kavelaars, J., Apr. 2010. Pencil-Beam Surveys for Trans-Neptunian Objects: Limits on Distant Populations. *ArXiv e-prints*.
- Peixinho, N., Lacerda, P., Jewitt, D., Nov. 2008. Color-Inclination Relation of the Classical Kuiper Belt Objects. *AJ*136, 1837–1845.
- Press, W. H., 2002. *Numerical recipes in C++ : the art of scientific computing*. Numerical recipes in C++ : the art of scientific computing by William H. Press. xxviii, 1,002 p. : ill. ; 26 cm. Includes bibliographical references and index. ISBN : 0521750334.
- Schlichting, H. E., Ofek, E. O., Wenz, M., Sari, R., Gal-Yam, A., Livio, M., Nelan, E., Zucker, S., Dec. 2009. A single sub-kilometre Kuiper belt object from a stellar occultation in archival data. *Nature*462, 895–897.
- Smith, J. A., Tucker, D. L., Kent, S., Richmond, M. W., Fukugita, M., Ichikawa, T., Ichikawa, S.-i., Jorgensen, A. M., Uomoto, A., Gunn, J. E., Hamabe, M., Watanabe, M., Tolea, A., Henden, A., Annis, J., Pier, J. R., McKay, T. A., Brinkmann, J., Chen, B., Holtzman, J., Shimasaku, K., York, D. G., Apr. 2002. The u'g'r'i'z' Standard-Star System. *AJ* 123, 2121–2144.
- Stansberry, J., Grundy, W., Brown, M., Cruikshank, D., Spencer, J., Trilling, D., Margot, J.-L., 2008. Physical Properties of Kuiper Belt and Centaur Objects: Constraints from the Spitzer Space Telescope. pp. 161–179.
- Stephens, D. C., Noll, K. S., Feb. 2006. Detection of Six Trans-Neptunian Binaries with NICMOS: A High Fraction of Binaries in the Cold Classical Disk. *AJ*131, 1142–1148.
- Stern, S. A., Sep. 1996. On the Collisional Environment, Accretion Time Scales, and Architecture of the Massive, Primordial Kuiper Belt. *AJ*112, 1203–+.
- Stern, S. A., Colwell, J. E., Aug. 1997. Accretion in the Edgeworth-Kuiper Belt: Forming 100-1000 KM Radius Bodies at 30 AU and Beyond. *AJ*114, 841–+.
- Tancredi, G., Fernández, J. A., Rickman, H., Licandro, J., Jun. 2006. Nuclear magnitudes and the size distribution of Jupiter family comets. *Icarus* 182, 527–549.
- Tegler, S. C., Romanishin, W., Oct. 2000. Extremely red Kuiper-belt objects in near-circular orbits beyond 40 AU. *Nature*407, 979–981.
- Trujillo, C. A., Brown, M. E., Feb. 2002. A Correlation between Inclination and Color in the Classical Kuiper Belt. *ApJL*566, L125–L128.
- Trujillo, C. A., Brown, M. E., Jun. 2003. The Caltech Wide Area Sky Survey. *Earth Moon and Planets* 92, 99–112.
- Trujillo, C. A., Jewitt, D. C., Luu, J. X., Feb. 2000. Population of the Scattered Kuiper Belt. *ApJL*529, L103–L106.
- Volk, K., Malhotra, R., Nov. 2008. The Scattered Disk as the Source of the Jupiter Family Comets. *ApJ*687, 714–725.
- Weissman, P. R., Snodgrass, C., Fitzsimmons, A., Lowry, S. C., Sep. 2009. The Size Distribution of Jupiter-Family Comet Nuclei. In: *AAS/Division for Planetary Sciences Meeting Abstracts*. Vol. 41 of *AAS/Division for Planetary Sciences Meeting Abstracts*. pp. 23.13–+.

Right Ascension	Declination
01:45:59.0	+10:03:00.0
01:46:29.7	+11:24:00.0
01:48:27.6	+10:30:00.0
01:48:59.1	+11:51:00.0
01:50:46.1	+10:30:00.0
01:51:07.5	+11:24:00.0
01:51:29.0	+12:18:00.0
01:51:39.8	+12:45:00.0
01:52:53.7	+10:03:00.0
01:53:15.5	+10:57:00.0
01:53:37.3	+11:51:00.0
01:53:48.3	+12:18:00.0
01:54:10.4	+13:12:00.0
01:55:34.1	+10:57:00.0
01:55:45.3	+11:24:00.0
01:56:30.2	+13:12:00.0
01:58:15.6	+11:51:00.0
01:58:50.0	+13:12:00.0
02:00:34.7	+11:51:00.0
02:07:32.1	+11:51:00.0
02:07:44.5	+12:18:00.0
02:07:56.8	+12:45:00.0
02:08:09.3	+13:12:00.0
02:09:51.3	+11:51:00.0
02:10:16.4	+12:45:00.0
02:12:23.2	+12:18:00.0
02:13:01.8	+13:39:00.0
02:15:08.7	+13:12:00.0
02:15:21.8	+13:39:00.0
02:17:15.2	+12:45:00.0
02:17:28.5	+13:12:00.0
02:21:54.3	+12:45:00.0
02:22:21.9	+13:39:00.0
02:22:35.8	+14:06:00.0
02:24:13.9	+12:45:00.0

Table 1: Suprime-cam Discovery field centers. Coordinates are presented in the J2000 epoch.

Object <sup>1</sup>	$r'_{Subaru}$	$r'_{SDSS}$	$(g_{SDSS} - r'_{SDSS})$	R (AU) <sup>2</sup>	i (°) <sup>2</sup>
obj_0	25.2 ± 0.1	25.0 ± 0.1	-	42.0 ± 3.0	10.0 ± 9.0
obj_1	24.55 ± 0.07	24.52 ± 0.07	-	42.0 ± 3.0	2.0 ± 8.0
obj_2	24.75 ± 0.08	24.72 ± 0.08	-	40.0 ± 3.0	20.0 ± 10.0
Nobj_3	23.99 ± 0.05	24.02 ± 0.05	0.46 ± 0.09	41.0 ± 3.0	4.0 ± 2.0
obj_4	24.71 ± 0.08	24.65 ± 0.08	-	43.0 ± 3.0	1.0 ± 6.0
Nobj_5	24.44 ± 0.07	24.45 ± 0.05	0.72 ± 0.09	43.5 ± 0.2	0.7 ± 0.03
obj_6	23.5 ± 0.04	23.47 ± 0.04	-	35.0 ± 3.0	6.0 ± 7.0
obj_7	24.83 ± 0.09	24.78 ± 0.09	-	41.0 ± 3.0	15.0 ± 10.0
Nobj_8	23.74 ± 0.04	23.73 ± 0.04	0.4 ± 0.1	45.0 ± 3.0	1.67 ± 0.01
obj_9	24.33 ± 0.07	24.29 ± 0.07	-	35.0 ± 2.0	2.0 ± 6.0
Nobj_10	23.02 ± 0.03	22.98 ± 0.03	0.7 ± 0.1	42.0 ± 3.0	6.0 ± 2.0
Nobj_11	24.19 ± 0.05	24.15 ± 0.05	0.6 ± 0.1	39.6 ± 0.4	7.3 ± 0.6
Nobj_12	23.55 ± 0.04	23.55 ± 0.04	0.53 ± 0.08	41.0 ± 3.0	30.0 ± 10.0
obj_13	24.63 ± 0.08	24.55 ± 0.07	-	40.0 ± 3.0	5.0 ± 8.0
obj_14	24.1 ± 0.05	24.07 ± 0.05	-	32.0 ± 2.0	3.0 ± 5.0
obj_15	24.9 ± 0.09	24.88 ± 0.09	-	30.0 ± 3.0	30.0 ± 20.0
obj_16	25.0 ± 0.1	24.96 ± 0.1	-	43.0 ± 3.0	1.0 ± 8.0
Nobj_17	21.65 ± 0.02	21.63 ± 0.02	0.6 ± 0.09	38.5 ± 0.1	9.6 ± 0.2
Nobj_18	24.43 ± 0.06	24.25 ± 0.06	0.9 ± 0.1	45.0 ± 2.0	0.97 ± 0.01
obj_19	24.88 ± 0.09	24.86 ± 0.09	-	36.0 ± 3.0	9.0 ± 7.0
Nobj_20	24.01 ± 0.05	24.0 ± 0.05	0.45 ± 0.09	44.0 ± 3.0	0.7 ± 0.2
Nobj_21	23.82 ± 0.04	23.79 ± 0.04	0.4 ± 0.09	39.0 ± 5.0	40.0 ± 30.0
obj_22	24.65 ± 0.08	24.62 ± 0.08	-	46.0 ± 3.0	10.0 ± 10.0
Nobj_23	23.96 ± 0.05	23.96 ± 0.05	0.5 ± 0.1	37.0 ± 2.0	1.7 ± 0.6
obj_24	24.75 ± 0.08	24.7 ± 0.08	-	42.0 ± 3.0	3.0 ± 8.0
obj_25	24.86 ± 0.09	24.82 ± 0.09	-	43.0 ± 3.0	3.0 ± 8.0
obj_26	25.0 ± 0.1	25.0 ± 0.1	-	43.0 ± 3.0	2.0 ± 8.0
Nobj_27	24.33 ± 0.06	24.38 ± 0.05	0.33 ± 0.07	38.0 ± 3.0	23.0 ± 9.0
2004 VT75 <sup>3</sup>	21.92 ± 0.03	21.9 ± 0.03	-	37.55	12.823
obj_29	23.65 ± 0.04	23.62 ± 0.04	-	30.0 ± 3.0	19.0 ± 9.0
Nobj_30	24.36 ± 0.06	24.29 ± 0.06	0.6 ± 0.1	46.0 ± 3.0	2.2 ± 0.8
Nobj_31	23.86 ± 0.04	23.78 ± 0.04	0.69 ± 0.09	43.0 ± 2.0	4.0 ± 1.0
Nobj_32	22.07 ± 0.02	22.08 ± 0.02	0.36 ± 0.09	39.39 ± 0.01	9.45 ± 0.01
Nobj_33	23.83 ± 0.04	23.79 ± 0.04	0.7 ± 0.1	38.0 ± 2.0	5.0 ± 2.0
Nobj_34	23.53 ± 0.05	23.54 ± 0.04	0.6 ± 0.1	37.0 ± 2.0	10.0 ± 4.0
Nobj_35	22.9 ± 0.03	22.88 ± 0.03	0.47 ± 0.08	36.2 ± 0.1	20.9 ± 0.4
obj_36	21.57 ± 0.02	21.55 ± 0.02	-	36.0 ± 3.0	14.0 ± 8.0
obj_37	22.51 ± 0.02	22.49 ± 0.03	-	32.0 ± 3.0	20.0 ± 10.0
obj_38	24.52 ± 0.07	24.49 ± 0.07	-	32.0 ± 2.0	11.0 ± 7.0
Nobj_39	23.9 ± 0.05	23.91 ± 0.04	0.58 ± 0.09	43.0 ± 3.0	2.9 ± 0.9
Nobj_40	23.25 ± 0.03	23.21 ± 0.03	0.66 ± 0.09	41.0 ± 2.0	2.6 ± 0.9
Nobj_41	23.77 ± 0.05	23.74 ± 0.05	0.66 ± 0.09	43.0 ± 3.0	2.6 ± 1.0
obj_42	24.26 ± 0.06	24.23 ± 0.06	-	32.0 ± 3.0	30.0 ± 10.0
obj_43	24.74 ± 0.08	24.72 ± 0.08	-	46.0 ± 3.0	8.0 ± 10.0
Nobj_44	24.18 ± 0.05	24.15 ± 0.05	0.38 ± 0.09	46.0 ± 3.0	2.8 ± 1.0
obj_45	24.55 ± 0.07	24.42 ± 0.07	-	47.0 ± 3.0	1.0 ± 10.0
Nobj_46	23.83 ± 0.04	23.8 ± 0.04	0.5 ± 0.1	37.0 ± 3.0	18.0 ± 7.0
Nobj_47	24.31 ± 0.06	24.27 ± 0.05	0.57 ± 0.09	43.0 ± 0.2	0.871 ± 0.002
obj_48	25.3 ± 0.2	25.1 ± 0.1	-	19.0 ± 4.0	40.0 ± 30.0
Nobj_49	23.85 ± 0.04	23.78 ± 0.04	0.56 ± 0.09	44.0 ± 3.0	7.0 ± 2.0

Nobj_50	23.57 ± 0.04	23.53 ± 0.04	0.65 ± 0.09	45.0 ± 2.0	4.0 ± 1.0
obj_51	25.0 ± 0.1	24.95 ± 0.1	-	34.0 ± 2.0	5.0 ± 6.0
obj_52	24.47 ± 0.07	24.41 ± 0.07	-	35.0 ± 3.0	4.0 ± 6.0
Nobj_53	23.92 ± 0.06	23.81 ± 0.06	0.7 ± 0.1	46.0 ± 3.0	2.2 ± 0.6
obj_54	24.95 ± 0.1	24.78 ± 0.09	-	43.0 ± 3.0	3.0 ± 8.0
obj_55	24.98 ± 0.1	24.93 ± 0.1	-	42.0 ± 3.0	2.0 ± 8.0
Nobj_56	24.35 ± 0.06	24.27 ± 0.06	0.6 ± 0.1	47.0 ± 3.0	3.0 ± 1.0
obj_57	24.84 ± 0.09	24.81 ± 0.09	-	43.0 ± 3.0	20.0 ± 10.0
obj_58	25.1 ± 0.1	24.9 ± 0.1	-	24.0 ± 3.0	30.0 ± 10.0
Nobj_59	24.44 ± 0.07	24.22 ± 0.05	0.66 ± 0.07	41.0 ± 0.1	2.14 ± 0.05
obj_60	24.05 ± 0.05	24.01 ± 0.05	-	28.0 ± 2.0	6.0 ± 5.0
Nobj_61	23.64 ± 0.05	23.57 ± 0.05	0.65 ± 0.09	42.0 ± 2.0	2.9 ± 0.9
Nobj_62	24.16 ± 0.07	24.21 ± 0.06	0.44 ± 0.09	43.0 ± 3.0	13.0 ± 5.0
obj_63	23.68 ± 0.04	23.65 ± 0.04	-	22.0 ± 2.0	14.0 ± 7.0
obj_64	24.54 ± 0.07	24.52 ± 0.07	-	42.0 ± 3.0	2.0 ± 7.0
Nobj_65	23.3 ± 0.03	23.27 ± 0.03	0.6 ± 0.1	43.5 ± 0.1	0.82 ± 0.01
obj_66	24.29 ± 0.06	24.26 ± 0.06	-	20.0 ± 8.0	70.0 ± 80.0
Nobj_67	24.44 ± 0.06	24.36 ± 0.06	0.67 ± 0.09	45.0 ± 3.0	1.6 ± 0.3
Nobj_68	23.81 ± 0.04	23.74 ± 0.04	0.64 ± 0.09	41.0 ± 3.0	3.0 ± 1.0
obj_69	24.65 ± 0.08	24.57 ± 0.08	-	42.0 ± 3.0	3.0 ± 8.0
obj_70	24.53 ± 0.07	24.5 ± 0.07	-	41.0 ± 3.0	4.0 ± 8.0
obj_71	23.85 ± 0.04	23.82 ± 0.05	-	34.0 ± 2.0	3.0 ± 5.0
Nobj_72	23.91 ± 0.05	23.88 ± 0.05	0.6 ± 0.1	44.0 ± 2.0	1.4 ± 0.3
Nobj_73	23.94 ± 0.05	23.83 ± 0.05	0.6 ± 0.1	44.0 ± 2.0	2.1 ± 0.8
Nobj_74	24.41 ± 0.08	24.68 ± 0.06	0.35 ± 0.08	41.0 ± 2.0	4.0 ± 1.0
obj_75	25.2 ± 0.1	25.1 ± 0.1	-	36.0 ± 3.0	1.0 ± 5.0
obj_76	24.68 ± 0.08	24.6 ± 0.08	-	42.0 ± 3.0	2.0 ± 8.0
Nobj_77	22.74 ± 0.03	22.72 ± 0.03	0.6 ± 0.1	42.3 ± 0.1	1.24 ± 0.02
Nobj_78	23.74 ± 0.04	23.71 ± 0.04	0.67 ± 0.09	42.0 ± 3.0	2.1 ± 0.3
obj_79	24.85 ± 0.09	24.78 ± 0.09	-	50.0 ± 3.0	1.0 ± 6.0
obj_80	24.58 ± 0.07	24.54 ± 0.07	-	42.0 ± 3.0	5.0 ± 8.0
obj_81	24.03 ± 0.05	24.01 ± 0.05	-	33.0 ± 2.0	6.0 ± 6.0
Nobj_82	24.19 ± 0.05	24.13 ± 0.05	0.78 ± 0.09	43.1 ± 0.1	0.31 ± 0.01
obj_83	23.06 ± 0.03	22.95 ± 0.03	-	35.0 ± 3.0	30.0 ± 10.0
obj_84	24.98 ± 0.1	24.94 ± 0.1	-	41.0 ± 3.0	2.0 ± 8.0
obj_85	24.54 ± 0.07	24.52 ± 0.07	-	30.0 ± 3.0	17.0 ± 9.0
Nobj_86	23.87 ± 0.04	23.84 ± 0.04	0.68 ± 0.09	42.0 ± 3.0	2.1 ± 0.6
obj_87	25.1 ± 0.1	25.1 ± 0.1	-	45.0 ± 3.0	8.0 ± 9.0

Table 2: Discovery Subaru magnitudes and Sloan magnitudes.

<sup>1</sup>Objects prefaced with N and D have follow-up observations in November and December respectively.

<sup>2</sup>Barycentric Distance and ecliptic inclination determined from *fit\_radec* (Bernstein and Khushalani, 2000).

<sup>3</sup>Object distance and inclination taken from the Minor Planet Center.



Table 3: Best-fit power-law parameters.

Sample	$\alpha$	$m_o(r')$	$P(\Delta > \Delta_{obs})$
<i>TNO</i>	$0.56 \pm 0.1$	$22.9 \pm 0.4$	0.64
<i>Cold<sub>F</sub></i>	$0.82 \pm 0.23$	$23.8 \pm 0.3$	0.28
<i>Cold</i>	$0.79 \pm 0.20$	$23.8 \pm 0.3$	0.47
<i>Hot<sub>F</sub></i>	$0.35 \pm 0.21$	$24.3 \pm 0.7$	0.75
<i>Hot</i>	$0.35 \pm 0.19$	$24.3 \pm 0.7$	0.65
<i>Close</i>	$0.40 \pm 0.15$	$23.6 \pm 0.6$	0.68

Table 4: The slopes of the *TNO*, *Hot*, *Cold*, and *Close* samples (rows 3, 5, and 6) are likely a few percent steeper than in actuality. This bias however, is much smaller than the uncertainties of those parameters (see Section 3.2).

## Fig. Captions

Fig. 1. Diagram of the fields observed for moving objects during the Subaru observations. These fields were chosen to avoid bright stars. The field center coordinates are presented in Table 1.

Fig 2. Point source full-width at half maximum versus hour angle of all Subaru discovery observations.

Fig 3. Extinction versus airmass for the Subaru discovery observations. Each point is the average difference in magnitude of bright stars between common fields; each of the 35 discovery triplets has two data points. The line is the best-fit linear extinction law, with slope 0.08 magnitudes per unit airmass. These data demonstrate the photometric nature of the discovery observations.

Fig 4. Detection efficiency versus artificial source  $r'_{Subaru}$  magnitude. Error-bars are 1-sigma poisson limits. Best-fit parameters of the efficiency function given by Equation 2 are presented at the top of the figure.

Fig 5. Detection efficiency versus artificial object inclination. From top to bottom, all planted sources, and those with  $r' < 23$ ,  $23 < r' < 24$ ,  $24 < r' < 26$ . This figure demonstrates that, given a particular object magnitude, our survey was equally sensitive to all inclinations.

Fig 6. Detection efficiency versus artificial object heliocentric distance. From top to bottom, all planted sources, and those with  $r' < 23$ ,  $23 < r' < 24$ ,  $24 < r' < 26$ . This figure demonstrates that, given a particular object magnitude, no significant variation of detection efficiency with distance is apparent. Exceptions are at the extrema of the survey; our search was only sensitive to objects with apparent motions  $0.2 - 10''/\text{hr}$  roughly corresponding to distances  $15 \leq r \leq 800$  AU.

Fig 7. Sloan colour versus inclination for those objects which received follow-up observations.

Fig 8. The differential luminosity functions of the various samples defined in Section 3.1 offset in units of 2 for clarity. Diamonds: *TNO*. Squares: *Cold<sub>F</sub>*. Triangles: *Hot<sub>F</sub>*. Circles: *Close*. Error-bars are the 1- $\sigma$  poisson limits for the number of objects in each bin. Lines are the best-fit power-laws, with values given in Table 3.

Fig 9. The 1 (solid), 2 (dashed) and 3- $\sigma$  (dotted) likelihood contours of the fits presented in Figure 8 and Table 3. The corresponding subsample is labeled in the top right of each panel.

Fig 10. Best-fit slopes  $\alpha$  of the *Cold* (squares) and *Hot* (circles) populations versus the inclination division  $i_{div}$  separating the two. Left is using only those objects with follow-up. Right is using all observations. The 1- $\sigma$  range in  $\alpha_{Close}$  is bracketed by the two horizontal lines.

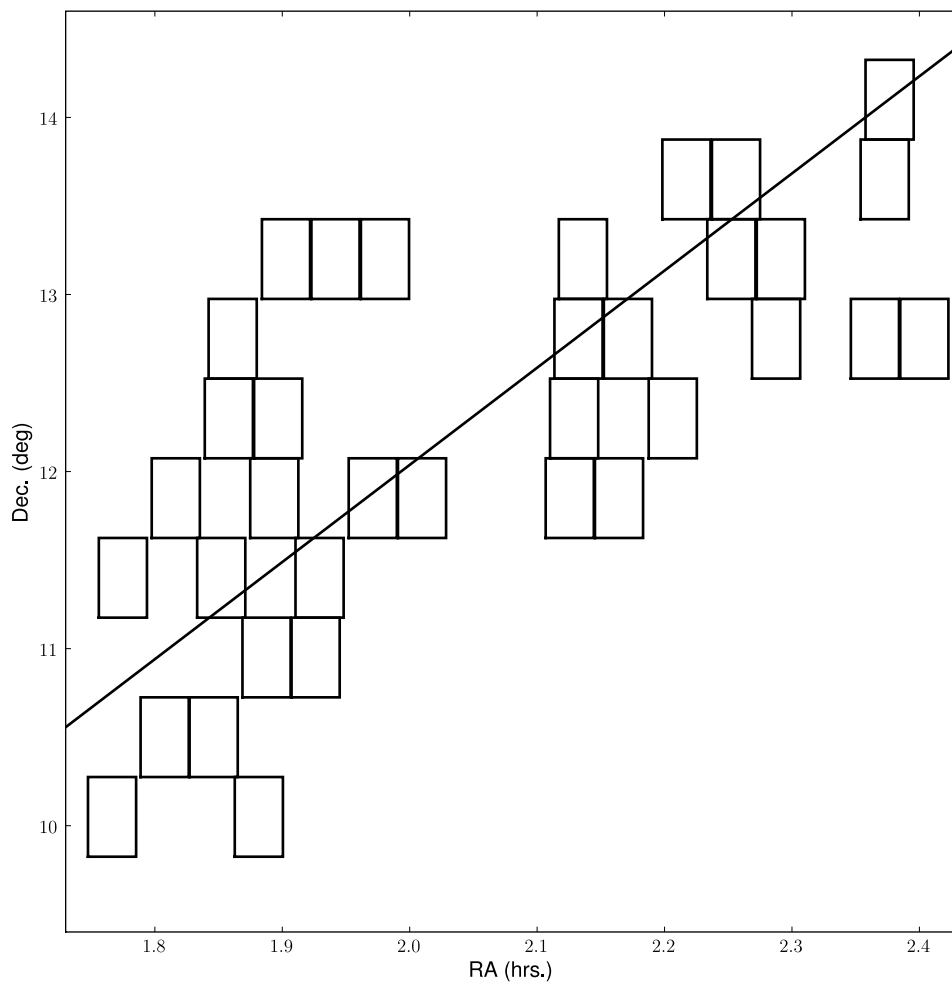


Figure 1:

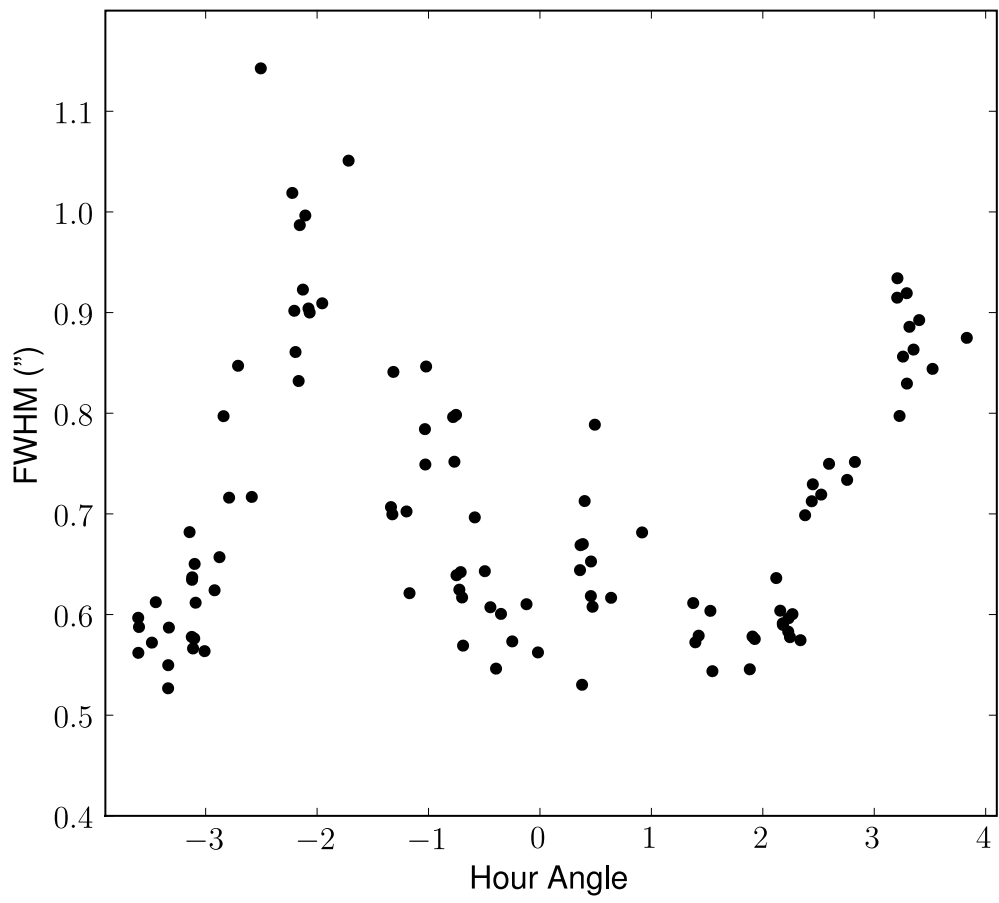


Figure 2:

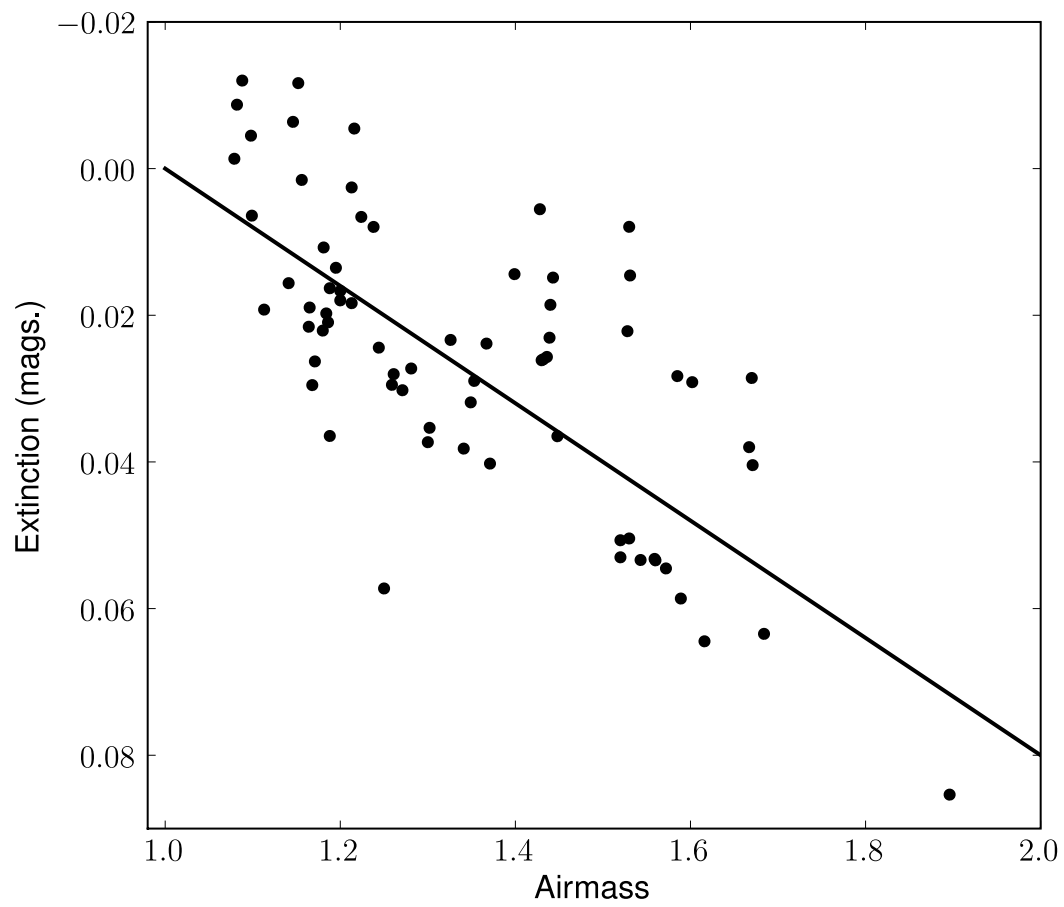


Figure 3:

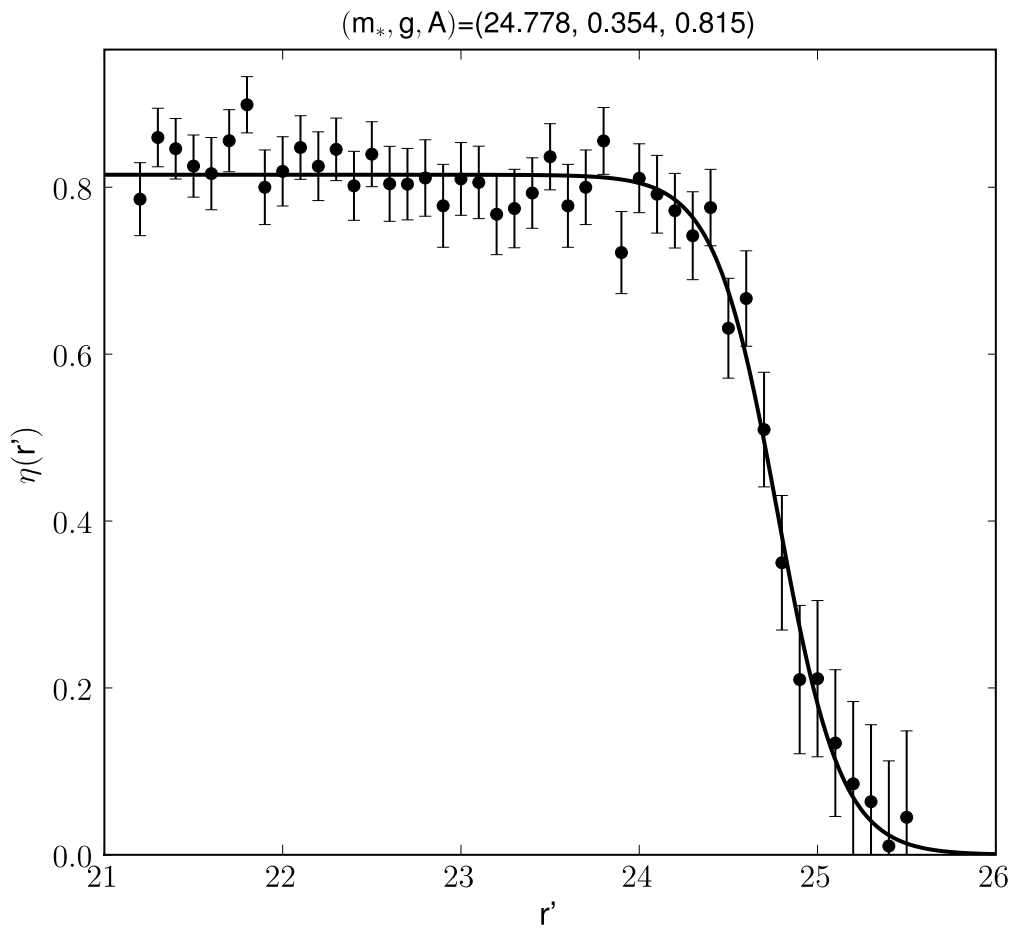


Figure 4:

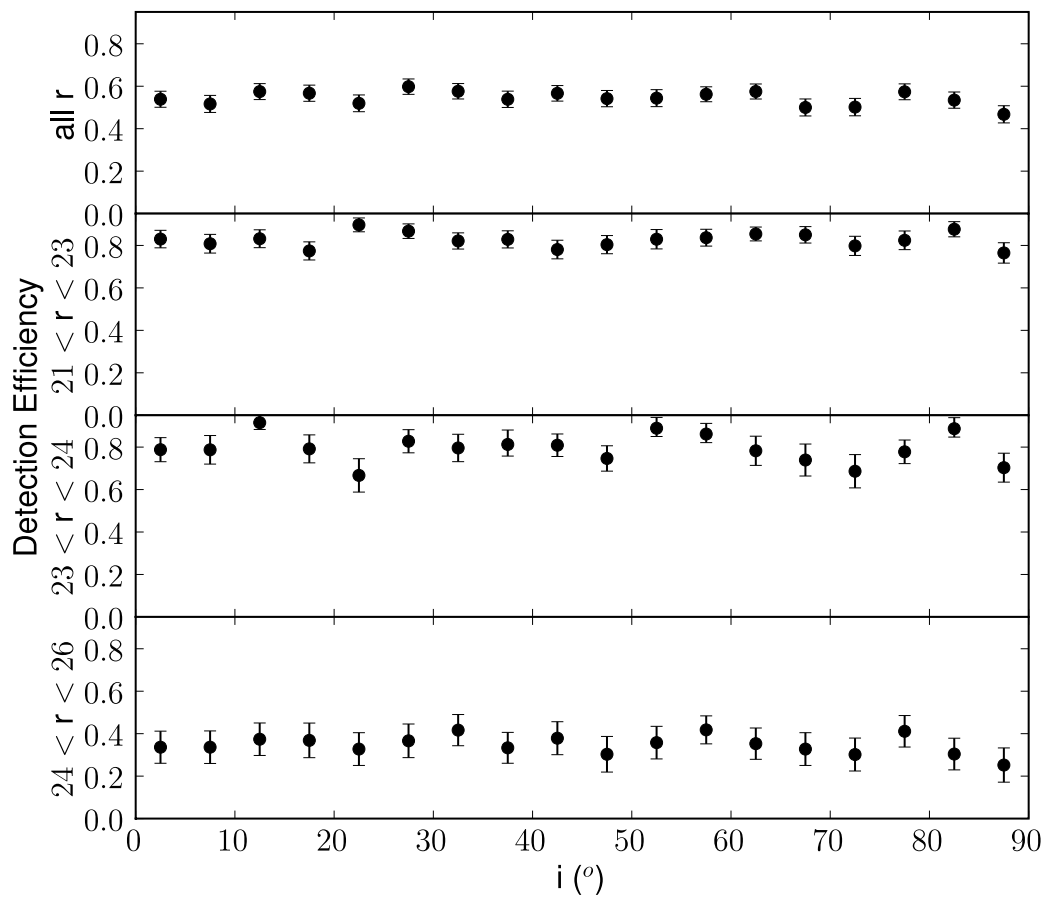


Figure 5:

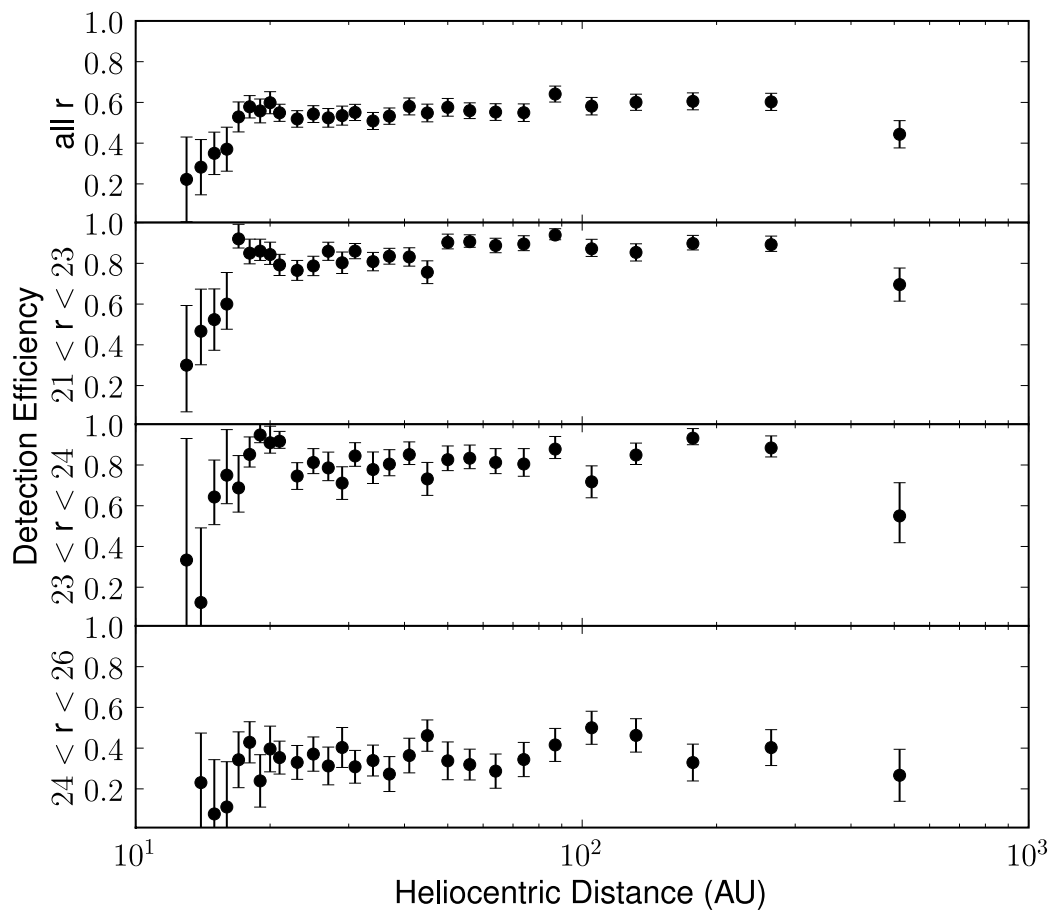


Figure 6:

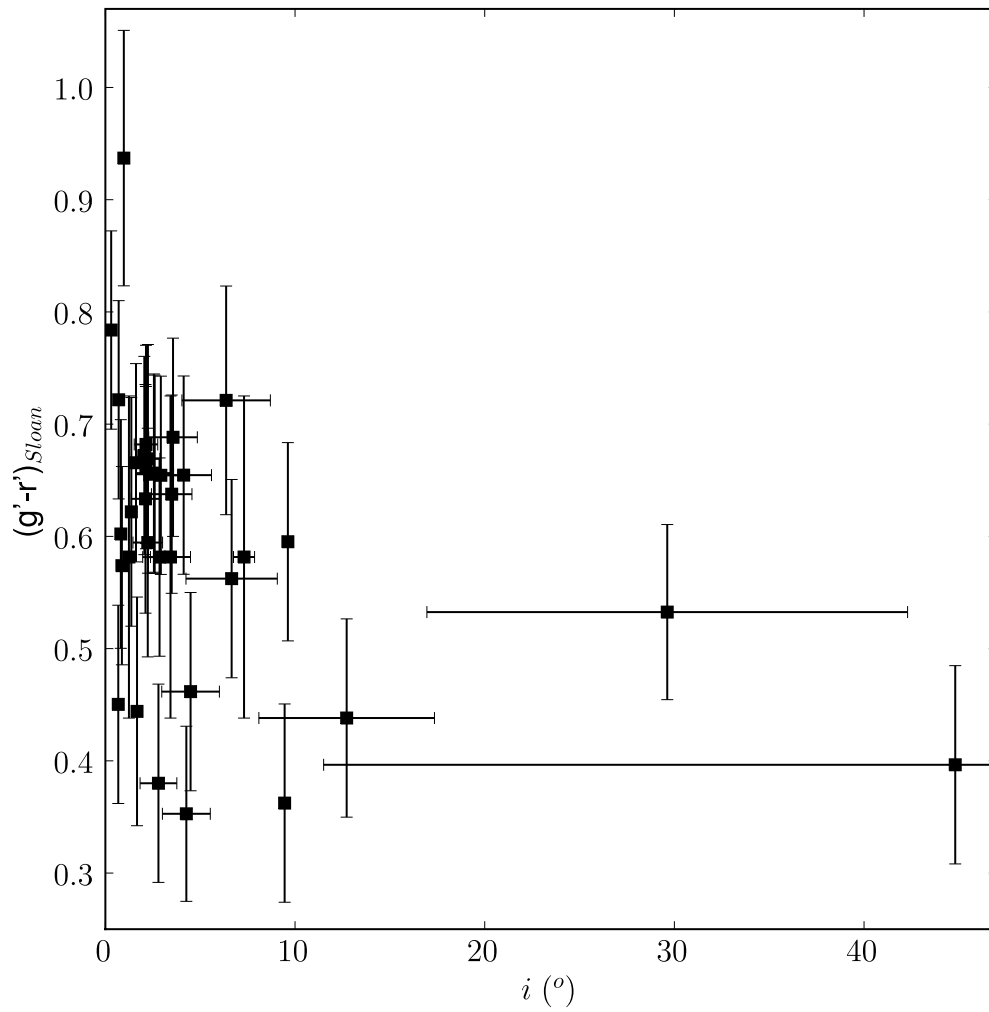


Figure 7:



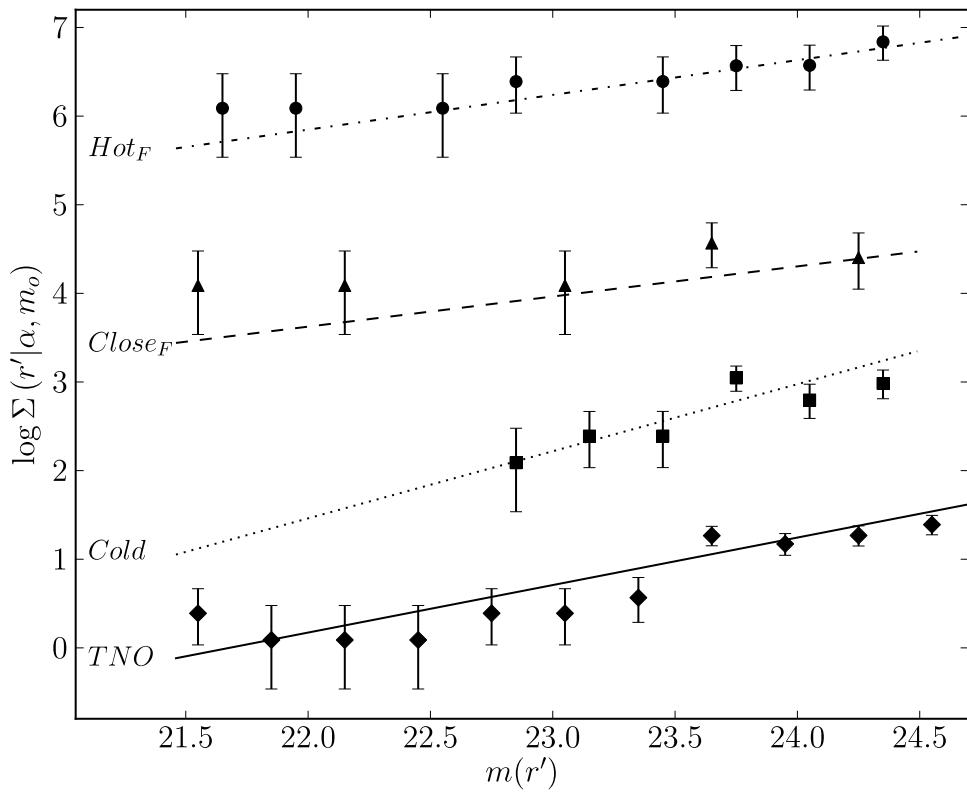


Figure 8:

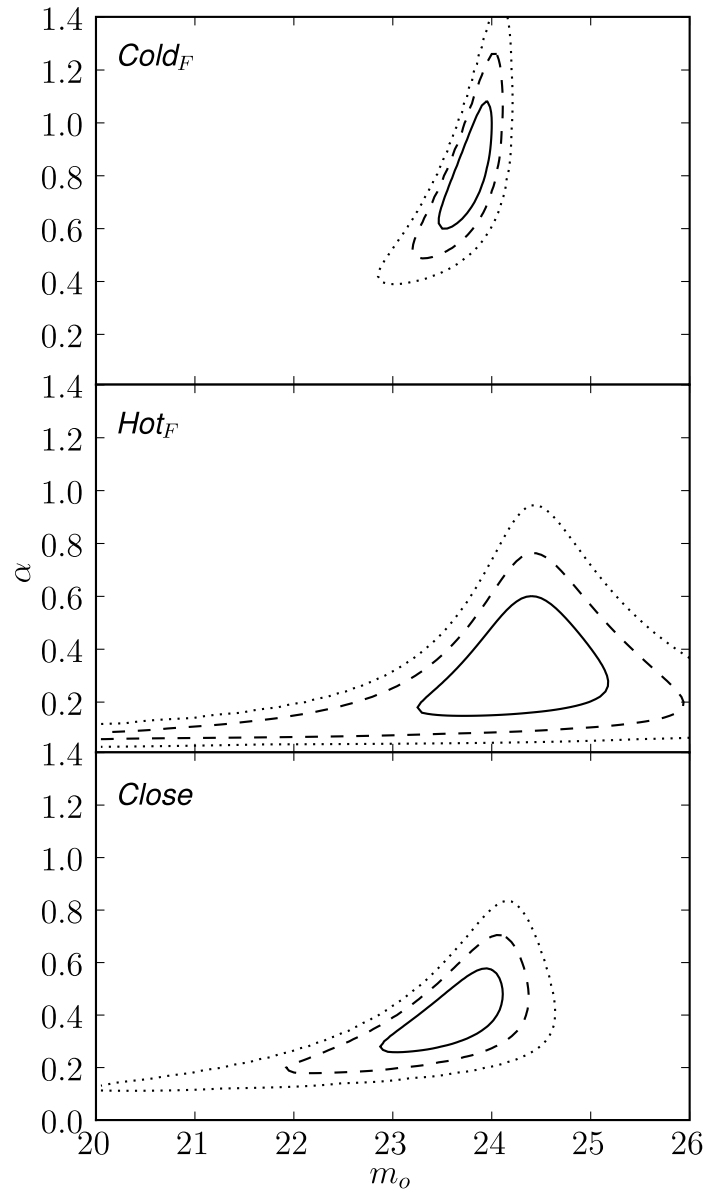


Figure 9:

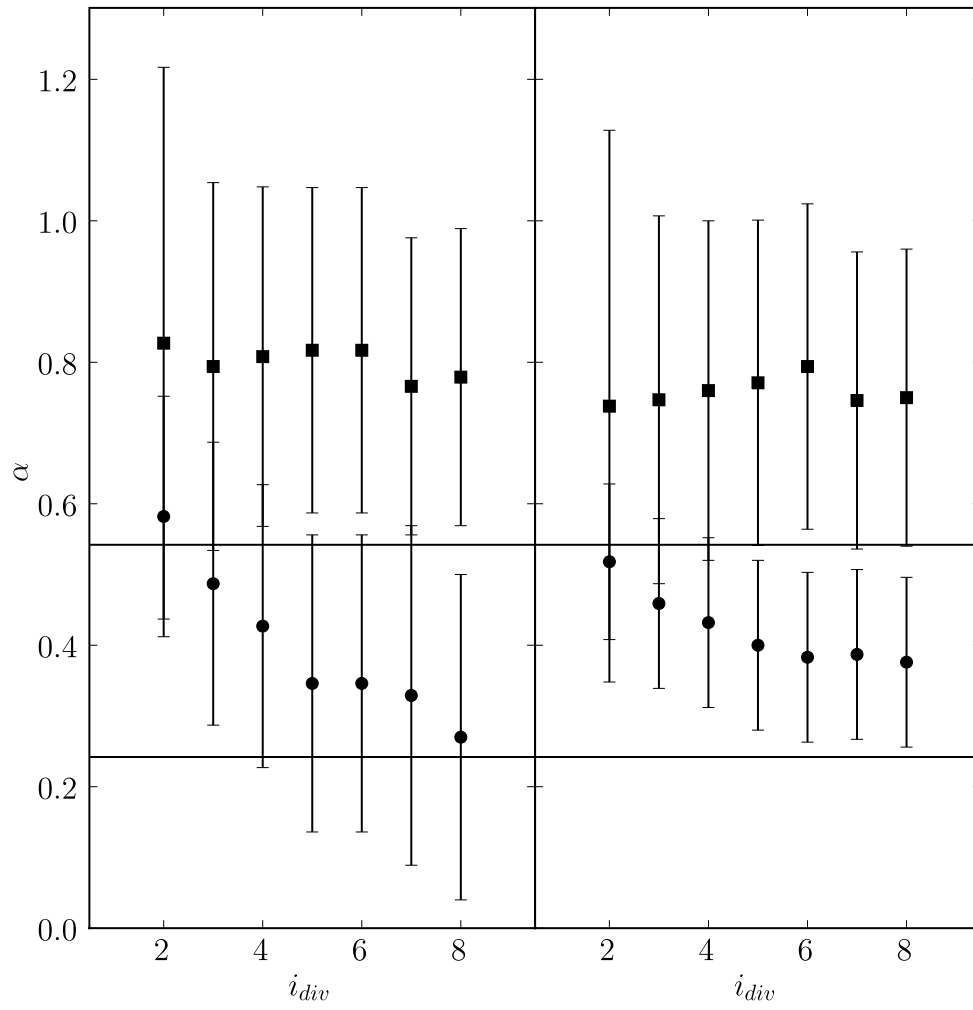


Figure 10: